Lithos 398–399 (2021) 106253

Contents lists available at ScienceDirect

Lithos

journal homepage: www.elsevier.com/locate/lithos

Research Article

Continental crust growth during the evolution of accretionary orogens: insights from the early Paleozoic granitoids in the Western Kunlun orogen, Northwest China

Kai Wu [a,*], Lipeng Zhang [b,c], Xiaoyan Jiang [d], Yuxiao Chen [e], Jia Guo [f], Weidong Sun [b,c], Qinglin Sui [b], Honglin Yuan [a,*]

[a] State Key Laboratory of Continental Dynamics, Department of Geology, Northwest University, Xi'an 710069, China
[b] Laboratory for Marine Mineral Resources, Pilot National Laboratory for Marine Science and Technology (Qingdao), Qingdao 266237, China
[c] Center of Deep Sea Research, Institute of Oceanography, Chinese Academy of Sciences, Qingdao 266071, China
[d] State Key Laboratory of Ore Deposit Geochemistry, Institute of Geochemistry, Chinese Academy of Sciences, Guiyang 550081, China
[e] Key Laboratory for Water Quality and Conservation of the Pearl River Delta, Ministry of Education, School of Environmental Science and Engineering, Guangzhou University, Guangzhou 510006, China
[f] College of Earth Sciences, Chengdu University of Technology, Chengdu 610059, China

ARTICLE INFO

Article history:
Received 28 September 2020
Received in revised form 20 May 2021
Accepted 23 May 2021
Available online 31 May 2021

Keywords:
Accretionary orogen
Crustal growth
Slab rollback
Western Kunlun
Proto-Tethys

ABSTRACT

Accretionary orogens are the primary sites for continental growth, but the rate and amount of crust generation throughout its evolution are poorly constrained. In this contribution, our new results about the genesis of two intermediate-felsic plutons are combined with a compiled granitoid dataset to evaluate the amount and rate of crustal growth throughout the evolution of the Western Kunlun orogen, which is a typical accretionary orogen associated with the consumption of the Proto-Tethys during the early Paleozoic. The ca.446 Ma Sanshili pluton was formed through interactions between metasomatized mantle wedge-derived oxidized magmas and the lower arc crust, as indicated by high whole-rock Mg#, high Ce^{4+}/Ce^{3+} ratios (308–861) of ca.446 Ma zircons, and the existence of inherited zircons with ages of 546–472 Ma. The Yirba dioritic to granodioritic pluton was emplaced at 474 ± 3 Ma. Samples from the Yirba pluton are characterized by high K_2O content, higher $Mg^{\#}$ (40–49) than pure crustal melts, slightly higher Y + Nb concentrations, and high Th/Nb ratios, and slightly enriched to depleted Hf–Nd isotopes. Combined with the presence of the 502–531 Ma inherited zircons, the Yirba pluton is suggested to from through differentiation of the metasomatized lithospheric mantle derived-magmas beneath the juvenile intra-oceanic arc in combination with crustal reworking during regional extensions. The Yirba pluton, together with contemporary A_1-type granites, thus marks an extension event at ca. 475 Ma in the Western Kunlun orogen. The compiled dataset reveals three magmatic flare-ups at 530–500 Ma, 480–470 Ma, and 445–430 Ma, corresponding to two slab rollback events and the slab break-off after the final closure of the Proto-Tethys. The three episodes of more intensive magmatism are associated with more radiogenic Hf–Nd isotopes and increased Nb/La and Nb/Y ratios, indicating more contributions from intraplate-like sources during lithospheric extensions. Meanwhile, element ratios (La/Yb, Sm/Yb, and Sr/Y) that are sensitive to crustal thickness are also elevated. These phenomena are consistent with rapid juvenile crust generation during extensional stages of accretionary orogens. Our study has also shown that the rate of new crust production is quite uniform for different extensional events. The crustal generation rate during slab break-off is much higher than that during slab rollback, although the proportions of juvenile inputs in granitoids formed during slab rollback are relatively higher. This may reflect extra inputs from partial melting of oceanic slabs and subducting sediments like those in continental collision zones and/or rapid asthenospheric upwelling coupled with enhanced crust reworking during slab break-off.

1. Introduction

There remains considerable debate concerning the origin of the continental crust and the mechanism and rate of crustal growth (Cawood et al., 2009; Hawkesworth et al., 2019; Niu et al., 2013). The similarity

* Corresponding authors.
E-mail addresses: wukai0302@gmail.com (K. Wu), hlyuan@nwu.edu.cn (H. Yuan).

https://doi.org/10.1016/j.lithos.2021.106253
0024-4937/

in geochemical compositions between the continental crust and subduction-related intermediate volcanic rocks suggests that continental growth is intimately bound up with subduction-related processes (Kelemen and Behn, 2016). Some studies argued for an episodic crustal growth mode based on radiogenic isotopes and episodic zircon age spectrum of orogenic granitoids (Cawood et al., 2009; Kemp et al., 2009). Such pulsed crustal extraction events have been attributed to mantle plume activities (Cawood et al., 2009). However, both plate tectonics at the Earth's surface and plume activities are primarily associated with heat loss from the Earth's mantle, and the former accounts for about 90% of the Earth's heat loss (Dhuime et al., 2018). In fact, the pre-3.0 Ga juvenile crust is mafic, while the post-3.0 Ga continental crust becomes intermediate (Dhuime et al., 2018). The ca.3.0 Ga pulse can also be explained by rapid recycling of pre-3.0 Ga mafic crust through subduction, and meanwhile, the modern continental crust began to form through subduction-related processes (Dhuime et al., 2018). A more comprehensive zircon Hf isotope dataset also constrains a smooth crustal growth curve, which favors the continuous crustal growth mode (Balica et al., 2020). Therefore, subduction-related magmatism at convergent margins is a fundamental process for modern continental crust growth (Cawood et al., 2009). Some studies also argued that the juvenile materials added into the continental crust through arc magmatism and the lateral accreted juvenile materials in accretionary orogens could be effectively counterbalanced by the recycled crustal materials at convergent margins (Cawood et al., 2009). However, there is increasing evidence that partial melting of the oceanic slab and sediments at continental collision zones and the opening of back-arc basins and subsequent back-arc closure in accretionary orogens are non-negligible processes that are responsible for new continental crust generation (Kemp et al., 2009; Niu et al., 2013). Moreover, post-collisional lithospheric mantle-derived igneous rocks with crustal isotopes are also significant juvenile additions to the continental crust (Moyen et al., 2017). Thus, igneous rocks in collisional and accretionary orogenic belts are ideal objects for studying crustal growth at convergent margins.

Collisional orogens refer to those mountain belts where the process of orogeny culminates with a continent-continent collision at the end of subduction (Cawood et al., 2009). In contrast, accretionary orogens involve repeated accretion of island arcs, oceanic plateaus, and microcontinents with continuing oceanic slab subduction beneath continental margins (Cawood et al., 2013). Accretionary orogens can be divided into retreating and advancing types, and an accretionary orogen usually undergoes multiple transitions between these two tectonic modes (Collins, 2002). In addition, accretionary orogens also have a collisional phase after the final closure of ocean realms (Cawood et al., 2009). Thus, granitoids formed at different tectonic circumstances during the evolution of accretionary orogens preserve much information about crustal growth and reworking. Therefore, it is an effective approach to ascertain relative amounts of new crust generation at different stages during the evolution of an accretionary orogen by tracking mantle input into granitic intrusions (Kemp et al., 2009).

The Western Kunlun orogen in central Asia links the Pamir syntaxis to the west and the East Kunlun orogen to the east (Yu et al., 2011), and was considered as the northwestern margin of the Tibetan Plateau (Wang et al., 2017; Xiao et al., 2003). Since the Western Kunlun mountain is an accretionary orogen during the Proto-Tethys Ocean evolution in the early Paleozoic (Xiao et al., 2003), it is of great importance in deciphering the early-stage crustal growth in the Tibetan Plateau (Ye et al., 2008). Abundant early Paleozoic granitoids developed in the Western Kunlun orogen in response to the Proto-Tethys evolution, which provides an ideal opportunity to explore the timing and geodynamic settings of crust generation. However, there are still many divergences concerning the age and petrogenesis of some granitic intrusions. Here, we present detailed zircon U–Pb age and Hf isotopic data, petrochemistry, and Sr–Nd isotopic compositions of two intermediate to felsic plutons (Sanshili and Yirba) to constrain their ages and petrogenesis. Our new results are then combined with a comprehensive geochronogy dataset of the early Paleozoic granitoids to figure out the magmatic episodes and a geochemical dataset to explore changes in the rate and amount of crustal growth during the evolution of the Western Kunlun orogen. In addition, our study is of great significance in identifying the geodynamic activities that promote crust generation in accretionary orogens.

2. Geological setting and sample descriptions

The Western Kunlun orogen is an important constituent part of the Central Orogenic System in eastern Asia (Wu et al., 2018; Xiao et al., 2005). It is separated from the Tarim Craton by the Kegang fault (Liao et al., 2010), and can be subdivided into the North Kunlun Terrane (NKT), the South Kunlun Terrane (SKT), the Tianshuihai Terrane (TSHT), and the Karakorum Terrane by the Oytag-Kudi suture, Mazha-Kangxiwa suture and Hongshanhu-Qiaoertianshan suture from north to south (Fig. 1). The breakup of Rodinia produced several branch oceans, one of which separated the SKT and the NKT as revealed by the Oytag-Kudi suture (Ye et al., 2008). The final closure of the Proto-Tethys at the Western Kunlun region occurred at 430–450 Ma (Wang et al., 2020). In contrast, the Mazha-Kangxiwa suture is associated with the Paleo-Tethys closure (Xiao et al., 2005).

The NKT is an uplifted terrane along the Tarim Craton's southwestern margin (Zhang et al., 2018b). The Precambrian metamorphic basement of the NKT is composed of the Paleoproterozoic Heluositan complex, the Mesoproterozoic greenschist- to amphibolite-facies sedimentary sequences (the KalaKashi Group) (Jiang et al., 1999), and the Late Neoproterozoic laminated carbonates and clastic rocks, which is covered by Devonian red molasse and Carboniferous-Permian shallow marine carbonate (Zhang et al., 2018b; Zhu et al., 2018). The Silurian to the Middle Devonian sedimentary sequences are absent, and the Upper Devonian terrestrial red molasse is only outcropped in the north margin of the Western Kunlun orogen and the south margin of the Tarim Craton (Liu et al., 2014).

The Kudi-Qimanyute suture comprises an alignment of ophiolite suites (e.g., the Kudi ophiolite and the Qimanyuter ophiolite) (Xiao et al., 2005). The Kudi ophiolite suite represents an obducted ophiolite that thrusted from the suture and emplaced on the South Kunlun terrane (Zhu et al., 2016), which consists of ultramafic rocks, a suit of volcanic and volcanoclastic rocks, and forearc sediments of the Yixieke Group (Yuan et al., 2003). Geochronological studies demonstrated that the age of the Kudi ophiolite is 525–490 Ma (Li and Zhang, 2014; Xiao et al., 2003). The Qimanyute ophiolite mainly comprises peridotite, layered gabbros, gabbros, diabase sheet, and basaltic pillow lavas. The ca.526 Ma layered gabbros in the Qimanyute ophiolites were intruded by Late Ordovician granitic rocks (Han et al., 2002).

The SKT comprises Precambrian metamorphic rocks, the Yixieke arc, the Kudi ophiolite, the Kudi genesis, the Xiaonanqiao arc, and the Pushou-Menggubao ophiolite suites (Yin et al., 2020; Yuan et al., 2005). Early studies considered the SKT as a drifted terrane from the Tarim Block, which shares a similar Precambrian basement with the NKT and the Tarim Block (Cui et al., 2007a). In this model, the outcropped Precambrian strata in the SKT contain the Pushou Group and the Sangzhutage Group in the north part and the Saitula Group in the south part separated by the Pushou-Menggubao ophiolitic melange (Cui et al., 2007b). The Pushou Group comprises high amphibolite-facies parametamorphic rocks, and the Sangzhutage Group consists of green schist-facies parametamorphic rocks (Cui et al., 2007b). A gneissic granodioritic pluton intruded into the Sangzhutage Group at ~505 Ma (Zhang et al., 2007). The Saitula Group is composed of schist and gneiss intercalated with amphibolite. The Pushou-Menggubao ophiolite comprises ultramafic rocks, gabbros, basalts, diabase, and siliceous rocks. Some basalts share similar geochemical features with oceanic-island basalts. Basaltic intrusion in the Pushou region and diabase in the Menggubao region represents a suite of typical arc magmatic rocks

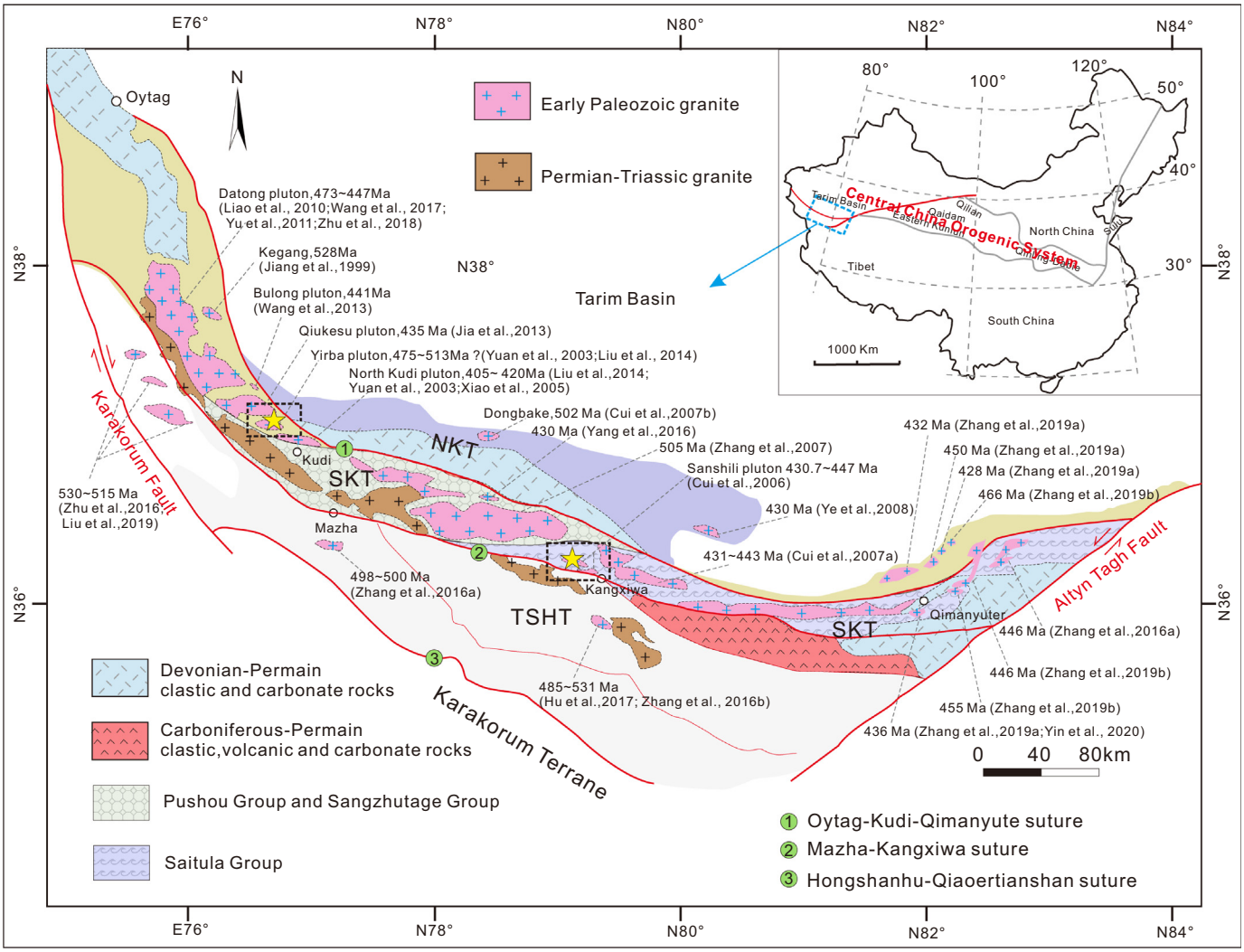

Fig. 1. Simplified geological map illustrating the distribution of the early Paleozoic granitoids in the Western Kunlun orogen (Modified from Zhang et al. (2019a)).

(Cui et al., 2007b). The age of the Pushou-Menggubao ophiolite is suggested to be the Early and Middle Ordovician (Cui et al., 2007b). However, the latest geological survey and geochronological data suggest that the so-called Precambrian basement rocks in the SKT were deposited during 600–480 Ma, and represent an early Paleozoic arc volcanic-sedimentary sequence (Zhang et al., 2018b).

The SKT and the TSHT are separated by the Mazha-Kangxiwa-Subashi suture, which consists of arc complexes, arc-related sedimentary rocks, and exotic blocks. The zircon SHRIMP U–Pb age of the hornblende-quartz diorite from the arc complexes is 338 ± 10 Ma (Li et al., 2007). The HP granulite within this suture has the protolith age of 456 ± 30 Ma and an amphibolite-facies retrograde metamorphic age of 177 ± 6 Ma (Yang et al., 2010).

The TSHT consists of meta-greywackes and limestone, which is in fault contact with the accretionary complexes (Zhang et al., 2018b). The TSHT was previously considered as an accretionary wedge associated with the late Paleozoic-early Mesozoic orogenic process (Xiao et al., 2005; Yin et al., 2020). Recent investigations on Paleoproterozoic metavolcanic rocks suggested the existence of a Precambrian basement beneath the TSHT (Zhang et al., 2018b), which implies that the TSHT is an independent terrane (Hu et al., 2016; Zhang et al., 2018b).

Granitic intrusions are widely distributed in the Western Kunlun orogen (Fig. 1) (Zhang et al., 2018b). The data source of the early Paleozoic granitoids discussed in this paper is available in Table S1. These granitoids are mainly exposed at the NKT and the SKT, while some recent studies reported many Cambrian intrusive and volcanic rocks in the TSHT, such as the Kelule, Nanpingxueshan, Ayilixi, and Warengzilafu plutons (Hu et al., 2017; Liu et al., 2019; Zhang et al., 2016a; Zhu et al., 2018). This paper focuses on two intermediate-felsic plutons (Sanshili and Yirba) in the Western Kunlun orogen, which were previously thought to be volcanic arc granitoids (Cui et al., 2006; Liu et al., 2014; Yuan et al., 2003).

The Sanshili pluton is composed of quartz-diorite and granodiorite. Samples from this pluton have a massive structure and medium-grained texture. Quartz-diorite samples consist of plagioclase (60–75%), K-feldspar (10–15%), quartz (6–18%), hornblende (ca. 10%) and biotite (ca. 5%) with minor magnetite, sphene and zircon (Fig. 2a). Granodiorite samples contain plagioclase (ca. 50%), K-feldspar (ca. 15%), quartz (ca. 22%), hornblende (ca. 10%) and biotite (ca. 2%) with minor accessory minerals (Fig. 2a). A previous study reported some mafic magmatic enclaves in the Sanshili pluton (Cui et al., 2006).

The Yirba pluton is about 20 km north of the Kudi village and covers an area of ca. 35 km^2. It intruded into the basic volcanic sequence of the Kudi ophiolite suite along the south margin (Liu et al., 2014; Xiao et al., 2003). The Yirba pluton is deformed and has a hornblende-biotite lineation parallel with the wall rocks (Yuan et al., 2003). The Yirba pluton comprises quartz diorite, granodiorite, and quartz monzonite. The quartz diorite is composed of plagioclase (55–70%), K-feldspar

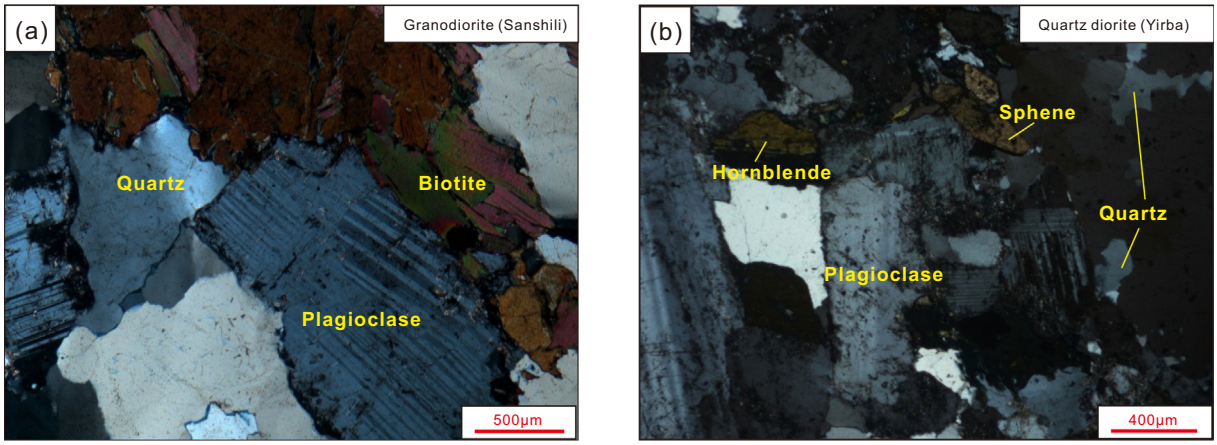

Fig. 2. Photomicrographs of representative samples from the Sanshili (a) and Yirba (b) plutons. (a) a granodiorite sample from the Sanshili pluton (87–447); (b) a quartz diorite sample from the Yirba pluton (87–233).

(15–20%), quartz (5–20%), hornblende (ca. 10%) and biotite (ca. 5%) (Fig. 2b). Granodiorite consists of plagioclase (ca. 50%), K-feldspar (15%), quartz (ca. 21%), hornblende (ca. 10%) and minor biotite. The quartz monzonite sample contains plagioclase (ca. 40%), K-feldspar (ca. 35%), quartz (ca. 12%), hornblende (ca. 10%), and biotite (ca. 5%). Accessory minerals include apatite, sphene, magnetite, and zircon. Zircon crystals separated from a granodiorite sample (87–447) from the Sanshili pluton and a quartz diorite sample (87–232) are used for zircon dating.

3. Analytical methods

3.1. Zircon U–Pb dating

Zircon U–Pb dating for the host rock was performed using LA-ICP-MS at the State Key Laboratory of Isotope Geochemistry, Guangzhou Institute of Geochemistry, Chinese Academy of Sciences (SKLIG-GIG-CAS). An Agilent 7900 ICP-MS coupled with a Resonetics RESOlution S155 laser-ablation system was used for zircon U–Pb dating and trace element analyses. The instrument conditions were set to 85 mJ laser energy, a repletion rate of 8 Hz, 31 μm spot size in diameter, and 45 s ablation time (Li et al., 2012). Helium was used as carrier gas sampling ablating aerosols to the ICP source. TEMORA and NIST SRM 610 were used as the external calibration standard for zircon U–Pb ages and zircon trace element contents, respectively. The standard reference zircons analyzed for this study are Qinghu and Plešovice. The mean $^{206}Pb/^{238}U$ age of the analyzed Qinghu zircons is 159 ± 2 Ma, and that of the Plešovice is 338 ± 4 Ma, which is indistinguishable from the recommended values (Li et al., 2013; Sláma et al., 2008). Zircon ages and trace element concentrations were processed with ICPMSDataCal 7.2 (Liu et al., 2008).

3.2. Zircon Hf isotopes

In-situ Lu–Hf isotopic compositions of zircons were analyzed using LA-MC-ICPMS at SKLIG-GIG-CAS, where a Thermo Finnigan Neptune multi-collector inductively coupled mass spectrometry (MC-ICP-MS) was coupled with a RESOlution M50 Laser ablation system. Lu–Hf isotope analyses were conducted on the same zonation of zircon domains previously ablated for U–Pb ages. The spot size is 44 μm in diameter. The instrument conditions are as follows: ablation time of 60s, 20 J/cm^2 energy, and a repletion rate of 8 Hz. Refer to Zhang et al. (2015) for more details. Multiple measurements of Plešovice in our experiments yielded a $^{176}Hf/^{177}Hf$ ratio of 0.282479, which is consistent with Sláma et al. (2008). The ^{176}Lu decay constant of $1.867*10^{-11}$ yr^{-1}was adopted to calculate the initial $^{176}Lu/^{177}Hf$. The $\varepsilon_{Hf}(t)$ was calculated relative to the chondritic reservoir with $^{176}Lu/^{177}Hf = 0.0336$ and $^{176}Hf/^{177}Hf = 0.282725$ (Bouvier et al., 2008). The Hf model age (T_{DM}) was calculated by assuming $^{176}Lu/^{177}Hf = 0.0384$ for the depleted mantle reservoir.

3.3. Whole-rock major and trace elements

Major and trace elements were measured at the SKLIG-GIG-CAS. Fresh samples were first crushed into small pieces, washed, and then powered into 200 mesh. Then 0.51–0.53 g powers were fluxed with $Li_2B_4O_7$ to make homogeneous glass disks at 1050–1100 °C. The major element contents were obtained by analyzing these glasses with X-ray fluorescence spectrometry. The analytical errors for major elements are better than 1%. The trace element analyses were carried out by ablating fluxed glass disks (with the sample to $Li_2B_4O_7$ of 1:3) using LA-ICPMS. An Agilent 7500 ICP-MS is coupled with a Resonetics RESOlution M-50 ArF-Excimer laser-ablation system. Laser energy was set to 80 mJ with a repetition rate of 6 Hz and a spot size of 69 μm. NIST 610 was used as an external standard and ^{29}Si as an internal standard for trace element analysis. More details about trace element analysis are available in Li et al. (2012). Data processing is carried out with ICPMSDataCal 7.2 (Liu et al., 2008).

3.4. Whole-rock Sr–Nd isotope

Whole-rock Sr–Nd isotope compositions were measured by a Multi-collector Inductively-Coupled plasma Mass Spectrometry (MC-ICP-MS) at University of Science and Technology of China. Chemical separation and purification were conducted at SKLIG-GIG-CAS following Liang et al. (2003) and Wei et al. (2002). An international standard BHVO-2 was used as the standard solution for isotopic ratio analysis. Multiple measurements of BHVO-2 in our experiments yielded $^{87}Sr/^{86}Sr = 0.703609$, $^{143}Nd/^{144}Nd = 0.512978$, which is consistent with the recommended values from the literature (Wei et al., 2002). The Rb, Sr, Sm, and Nd concentrations measured by ICP-MS were used to calculate the initial isotopic ratios.

4. Results

4.1. Zircon U–Pb geochronology

The LA-ICP-MS dating results are listed in Table S2. Zircon crystals from the Sanshili granodiorite (87–447) are transparent, colorless, and euhedral with length/width ratios of 2:1 to 3.5:1. As shown in Fig. 3a,

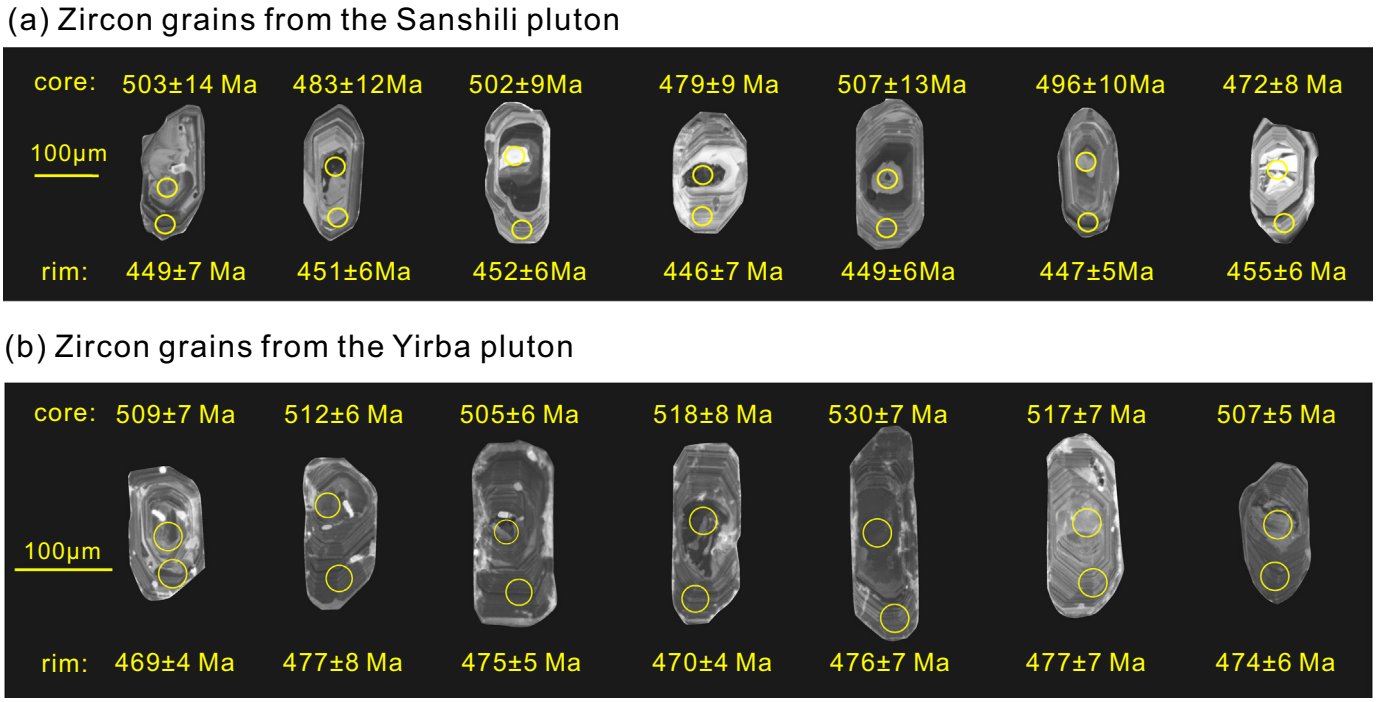

Fig. 3. Representative cathodoluminescence (CL) images of zircons from the Sanshili and the Sanshili plutons.

zircon crystals in the Sanshili pluton show oscillatory magmatic zoning occasionally with inherited cores. Zircon domains with apparently oscillatory zonation contain 203–1131 ppm Th and 450–1975 ppm U with Th/U ratios of 0.45–0.79, suggesting that they belong to magmatic zircons (Hoskin and Schaltegger, 2003). Twenty spot analyses on these zircon domains yield a weighted mean $^{206}Pb/^{238}U$ age of 446 ± 3 Ma (2σ, MSWD = 0.67) (Fig. 4). The inherited cores have variable Th (141–1485 ppm), U (341–1935 ppm), and Th/U (0.28–0.77) ratios, and their $^{206}Pb/^{238}U$ ages have a relatively wide range from 546 Ma to 472 Ma. The obtained zircon U–Pb age (446 ± 3 Ma) for the Sanshili pluton agrees well with the previously reported zircon SHRIMP U–Pb age (447 ± 7 Ma) (Cui et al., 2006), which is interpreted as the crystallization age of the Sanshili pluton.

Zircons grains from the Yirba quartz diorite sample (sample 87–232) are all transparent, colorless, and euhedral crystals with length/width ratios of 2:1 to 4:1. They also occasionally display oscillatory magmatic zoning with inherited cores with dark or obscure CL features (Fig. 3b). The Th and U concentrations, and the Th/U ratios for zircons with apparent magmatic zoning range from 210 to 919 ppm, 559–1331 ppm, and 0.32–0.77, respectively. Twenty-two spot analyses on this type of zircons yield concordant $^{206}Pb/^{238}U$ ages varying from 469 Ma to 478 Ma with a weighted mean $^{206}Pb/^{238}U$ age of 474 ± 3 Ma (Fig. 5). The inherited cores also have variable concentrations of Th (213–991 ppm), U (385–1479 ppm), and Th/U ratios (0.34–0.77). Thirteen spot analyses on these cores yield an older weighted mean $^{206}Pb/^{238}U$ age of 513 ± 5 Ma (2σ, MSWD = 1.4). The SHRIMP U–Pb zircon age (513 ± 7 Ma) reported by Liu et al. (2014) is indistinguishable from the age of these inherited zircon cores. Therefore, the best estimation of the crystallization age of the Yirba pluton should be 475 ± 3 Ma.

4.2. Zircon Hf isotopic compositions

In situ zircon Lu–Hf isotope analysis was performed on the same area previously dated by LA-ICP-MS. The results are presented in Table S3 and graphically illustrated in Fig. 6. Zircon domains with oscillatory magmatic zoning from the Sanshili pluton have $^{176}Hf/^{177}Hf$ of 0.282280–0.282360, negative $\varepsilon_{Hf}(t)$ values of −8.1 to −5.2 and corresponding two-stage Hf model ages of 1656–1483 Ma. The $^{176}Hf/^{177}Hf$ of the inherited zircon cores vary from 0.282248 to 0.282345, with corresponding $\varepsilon_{Hf}(t)$ values of −8.6 to −4.9 and two-stage Hf model ages of 1680–1504 Ma.

Zircon domains with apparent oscillatory magmatic zoning from the Yirba pluton have variable $^{176}Hf/^{177}Hf$ ratios from 0.282404 to 0.282538, with corresponding $\varepsilon_{Hf}(t)$ varying from −3.1 to +1.8. The calculated two-stage Hf model ages (T_{DM2}) ranges from 1402 Ma to 1156 Ma. The $^{176}Hf/^{177}Hf$ ratios for their inherited cores are from 0.282374 to 0.282445, with corresponding $\varepsilon_{Hf}(t)$ varying from −3.7 to −1.0.

4.3. Whole-rock geochemistry

Major and trace element compositions of representative samples from the Yirba and Sanshili plutons are available in Table S4 (including data of the analyses on standards and duplicate samples). Samples from the Sanshili pluton have SiO_2 = 54.3–62.8 wt%, Al_2O_3 = 14.9–22.0 wt%, and CaO = 5.10–7.73 wt%, which are metaluminous (A/CNK = 0.73–0.89) and mostly plotted in the field of diorite and syeno-diorite in TAS (total alkalis versus SiO_2) diagram (Fig. 7). They are geochemically calc-alkaline in composition, and the MgO contents of these samples vary from 1.81 wt% to 6.23 wt% with corresponding $Mg^{\#}$ of 45–58. In primitive mantle normalized trace element spider diagram, they display similar distribution patterns with the upper continental crust (Fig. 8). Samples from the Sanshili pluton are light rare earth element-enriched with $(La/Yb)_N$ = 6.37–25.5 (Fig. 8).

Samples from the Yirba pluton are mostly plotted in the field of diorite, syeno-diorite, and quartz diorite (Fig. 7). They have variable SiO_2 from 53.5 wt% to 63.3 wt% with high Na_2O (2.43–4.61 wt%) and K_2O (2.07–4.66 wt%) contents, which are geochemically high-K calc-alkaline to shoshonitic series and metaluminous with A/CNK values ranging from 0.71 to 0.88. The MgO contents of the Yirba pluton vary from 1.58 wt% to 4.24 wt%, with $Mg^{\#}$ of 39–49. Their chondrite-normalized REE distribution patterns are highly fractionated with $(La/Yb)_N$ of 14–35 and δEu of 0.64–0.90 (Fig. 8). In the primitive mantle-normalized trace element spider diagram, these samples

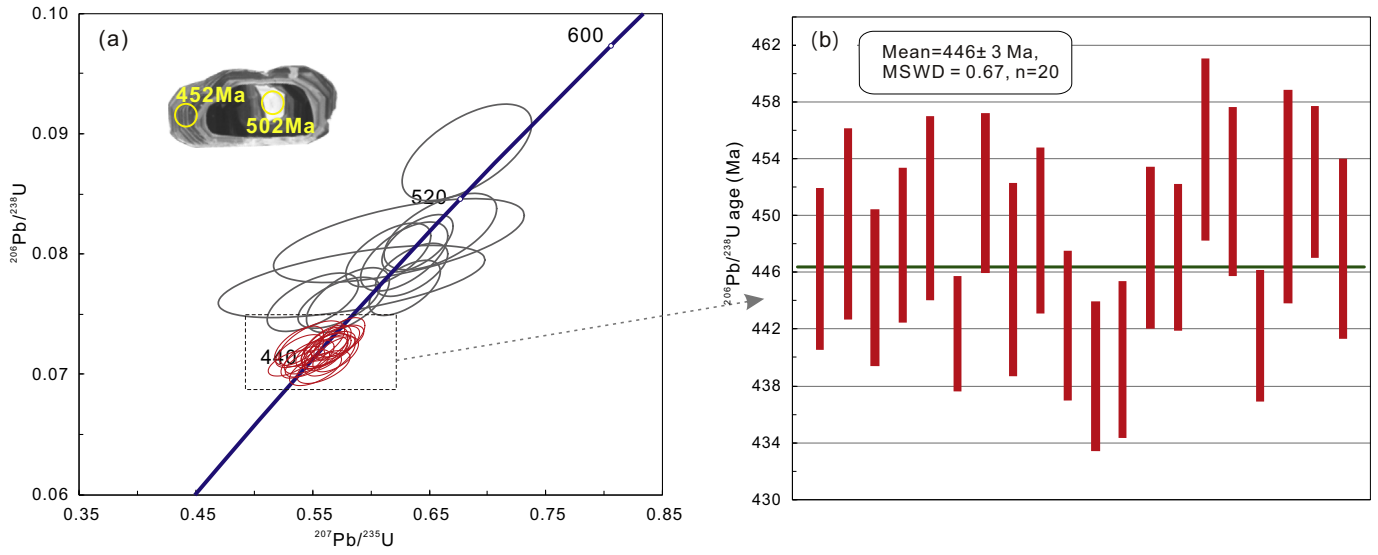

Fig. 4. Zircon U–Pb concordia diagrams for the Sanshili pluton.

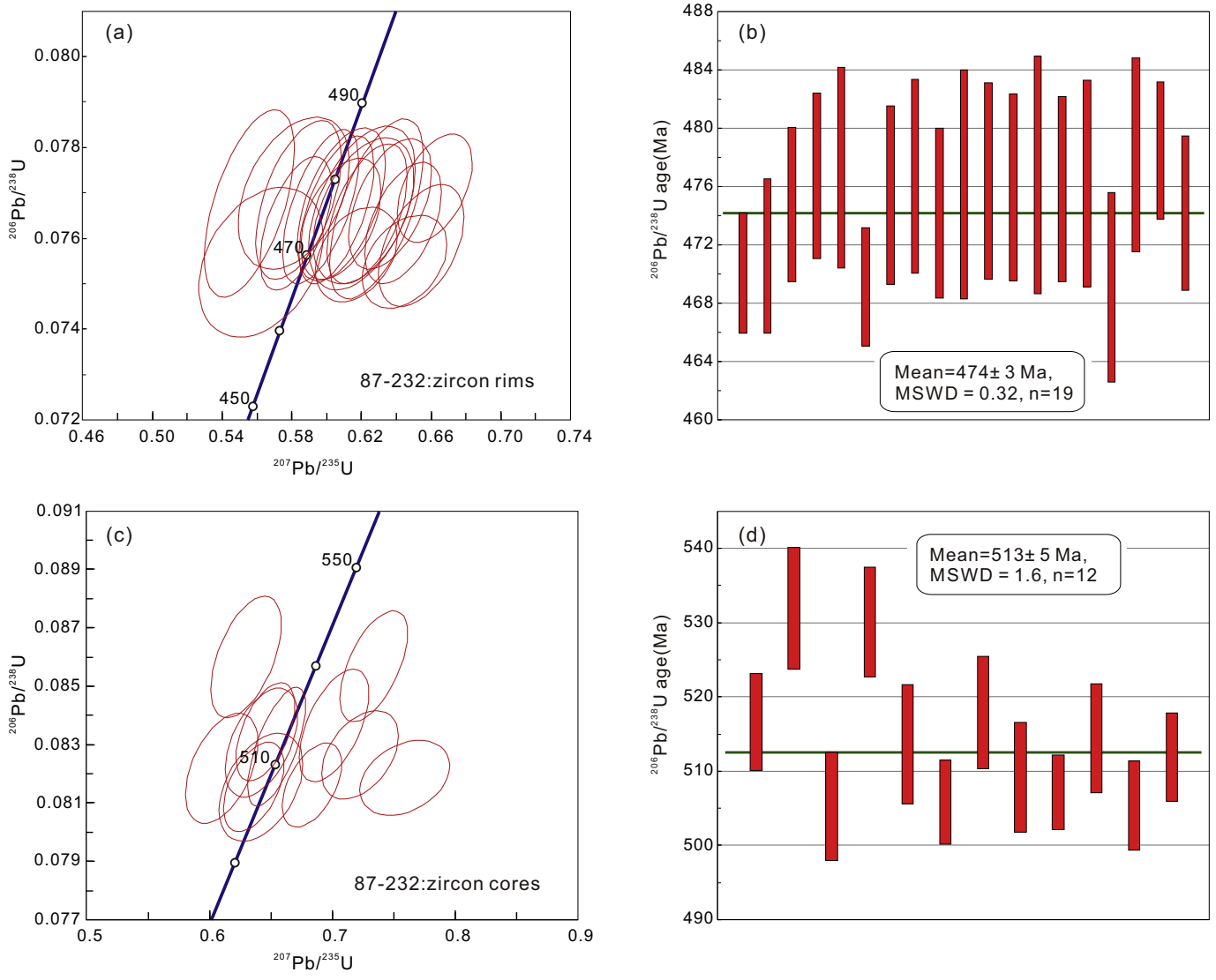

Fig. 5. Zircon U–Pb concordia diagrams for the Yirba pluton.

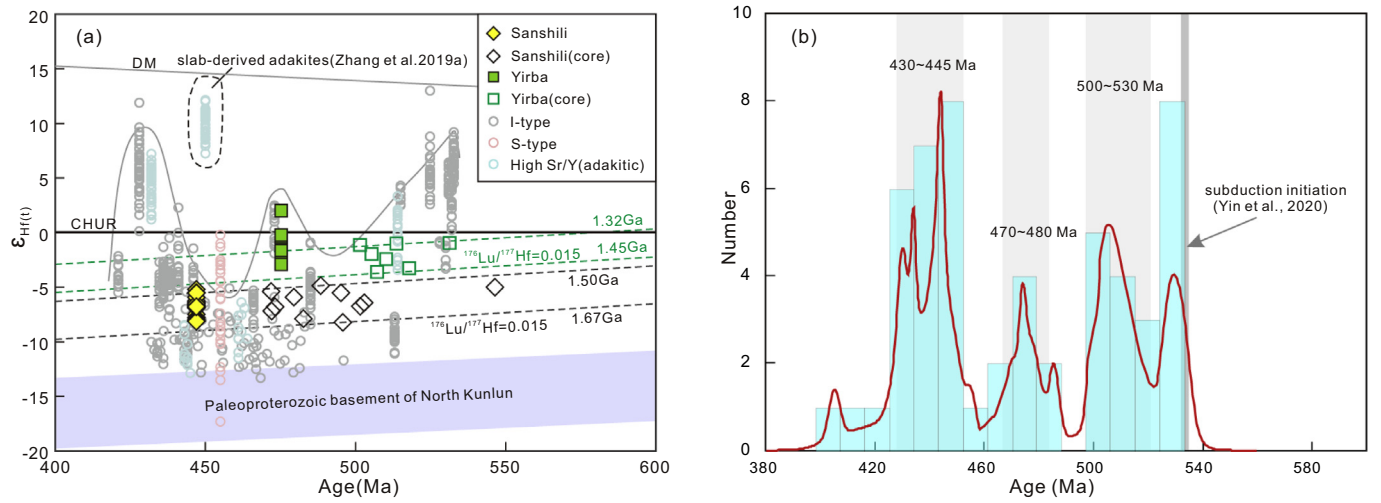

Fig. 6. Zircon Hf isotopic compositions for samples from the Sanshili and Yirba plutons. The data source of the plotted Early Paleozoic granitoids in the Western Kunlun orogen is available in Table S1. The field of the Paleoproterozoic basement of North Kunlun is from Zhang et al. (2017).

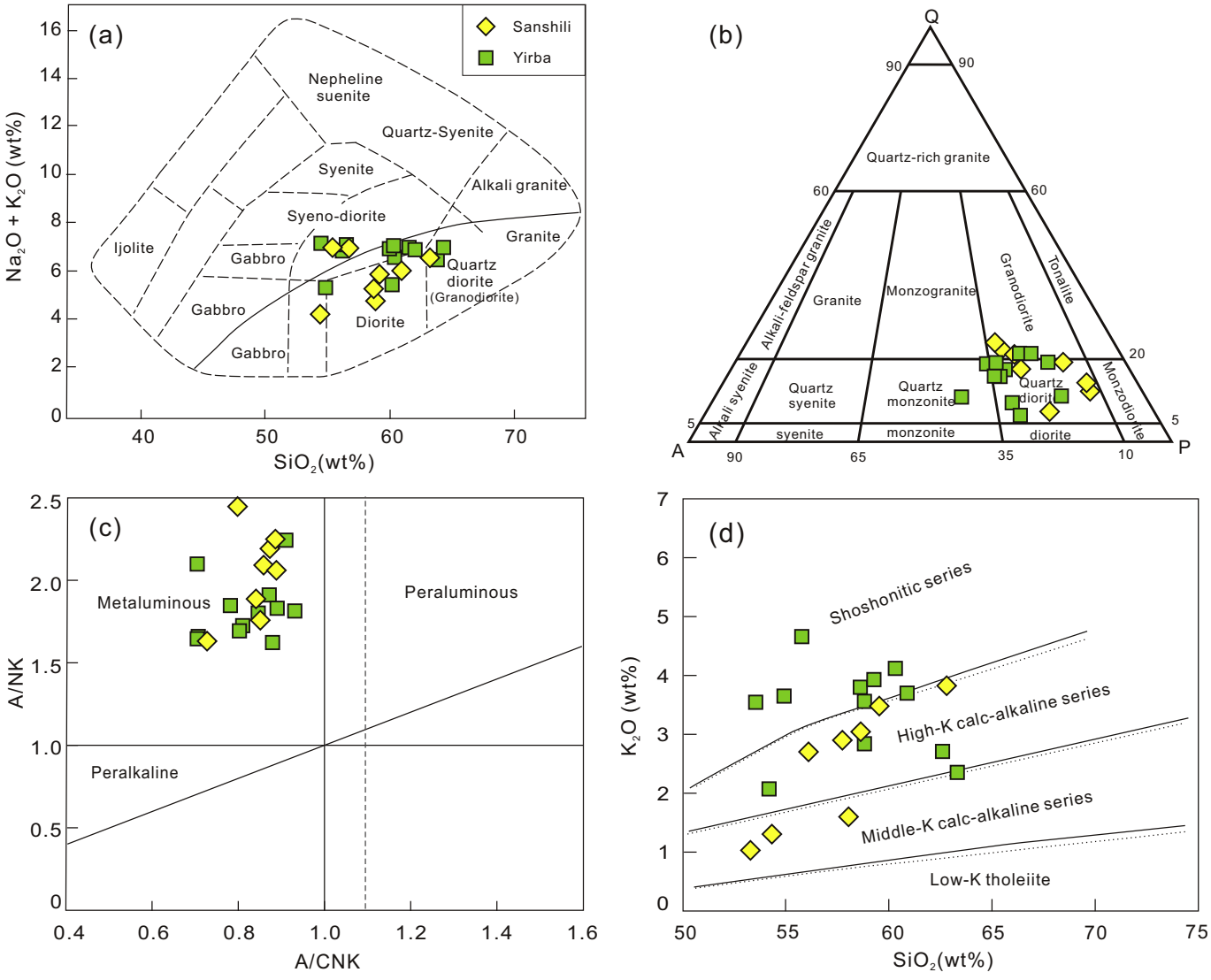

Fig. 7. TAS diagram (a), QAP ternary diagram (b), A/NK versus A/CNK diagram (c), and K_2O versus SiO_2 diagram (d) for samples from the Sanshili and Yirba plutons.

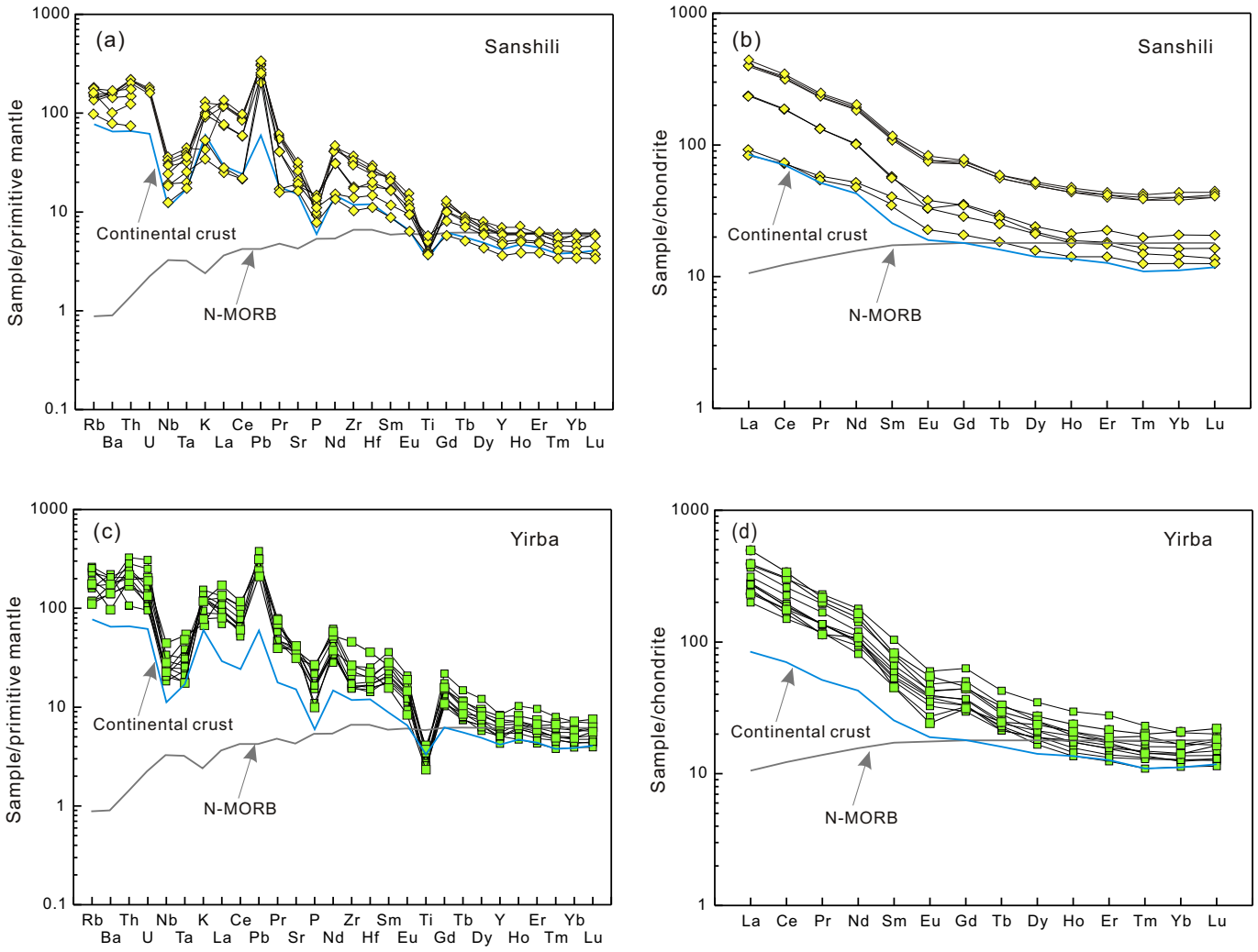

Fig. 8. Primitive mantle-normalized trace element and chondrite-normalized REE distribution diagrams for samples from the Sanshili and the Yirba plutons. Data used for normalization are from Sun and Mcdonough (1989). The average continental crust and N-MORB are from Rudnick and Gao (2003), and Sun and Mcdonough (1989).

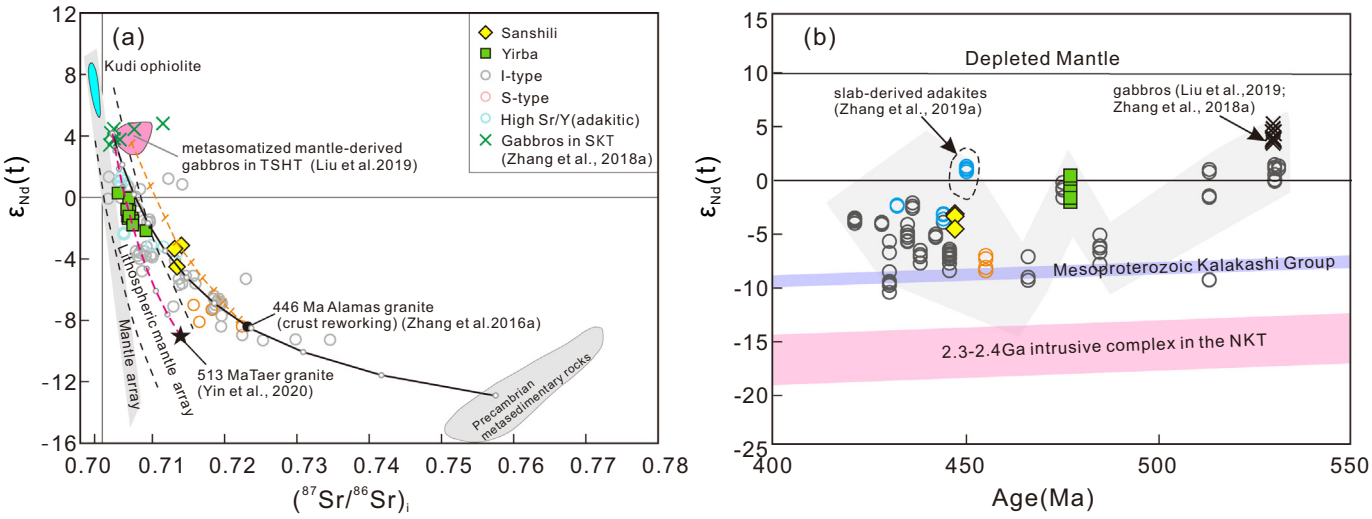

Fig. 9. (a) Sr–Nd isotopic compositions for samples from the Sanshili and the Yirba plutons. The data source for the Sr–Nd isotopic compositions of the Early Paleozoic granitoids in the Western Kunlun orogen can be found in Table S1. The Field of Precambrian metasedimentary rocks, basaltic rocks in the Kudi ophiolite, and subduction initiation gabbros are from Jia et al. (2013), Liu et al. (2014), and Liu et al. (2019). The lithospheric mantle-derived melts field is from worldwide alkali basalts, kimberlites, and lamproites (Davies and von Blanckenburg, 1995). (b) Changes in the Nd isotopic compositions of the Early Paleozoic granitoids. The field of Mesoproterozoic Kalakashi Group and 2.3–2.4 Ga intrusive complex in the NKT is from Ye et al. (2008).

display a similar distribution pattern with that of the upper crust except for the slightly positive K anomalies. They are enriched in large ion lithophile elements (e.g., Rb, Ba, Sr, Th, U, K, and Pb) and depleted in high field strength elements (e.g., Nb, Ta, and Ti).

4.4. Sr–Nd isotopic compositions

The Sr–Nd isotopic data are also available in Table S4. Our newly obtained data and those from the literature are all shown in Fig. 9. Samples from the Sanshili pluton display relatively homogeneous Sr–Nd isotopic compositions with initial $^{87}Sr/^{86}Sr$ ratios of 0.7131–0.7140 and $\varepsilon_{Nd}(t)$ of −4.5 to −3.1. Compared with samples from the Sanshili pluton, samples from the Yirba pluton (including literature data) have generally lower and more variable $(^{87}Sr/^{86}Sr)_i$ from 0.7052 to 0.7091, but higher $\varepsilon_{Nd}(t)$ of −2.2 to +0.3.

5. Discussion

5.1. Petrogenesis of the Sanshili pluton

The Sanshili pluton is mainly composed of quartz diorite and granodiorites. Samples from this pluton are characterized by high $(^{87}Sr/^{86}Sr)_i$ (0.7131–0.7140), low $\varepsilon_{Nd}(t)$ (−4.5 to −3.1) and zircon $\varepsilon_{Hf}(t)$ (−8.1 to −5.2), which indicates that they were not derived from juvenile crustal materials. Some zircons from the Sanshili pluton contain inherited cores (Fig. 3), whose ages span a wide range from 546 Ma to 472 Ma. The U concentrations, Th/U ratios, and $\varepsilon_{Hf}(t)$ values of these inherited cores are all indistinguishable from those of zircon crystals with ages of ca. 446 Ma (Fig. 6a and 10). However, the Ce^{4+}/Ce^{3+} ratios of ca.446 Ma zircon domains (308–861) are much higher than those of the inherited zircon cores (⟨300) (Fig. 10). Since preferentially partitioning Ce^{4+} into zircon crystal structure relative to Ce^{3+} makes Ce^{4+}/Ce^{3+} ratios of zircon a helpful indicator of magma oxygen fugacity (Ballard et al., 2002; Trail et al., 2012), the high Ce^{4+}/Ce^{3+} ratios of ca.446 Ma zircons indicates the involvement of oxidized components in generation of the Sanshili pluton.

The quartz diorite and granodioritic samples from the Sanshili pluton display arc-like geochemical features (e.g., enriched LILE and depleted HFSE) (Fig. 8). It has been proposed that tonalitic and granodioritic intrusions at the convergent margins can be produced through fluid-fluxed melting of the mafic lower arc crust (Collins et al., 2016). However, the fluid-fluxed melting model is inappropriate to interpret the origin of the Sanshili pluton, although the high oxygen fugacity recorded by the ca.446 Ma zircon crystals can be plausibly explained by additions of exsolved hydrous fluids from underplated magmas. This is because the Sanshili pluton has slightly higher Mg# (45–58) than pure crustal melts (Fig. 11), and there exist abundant

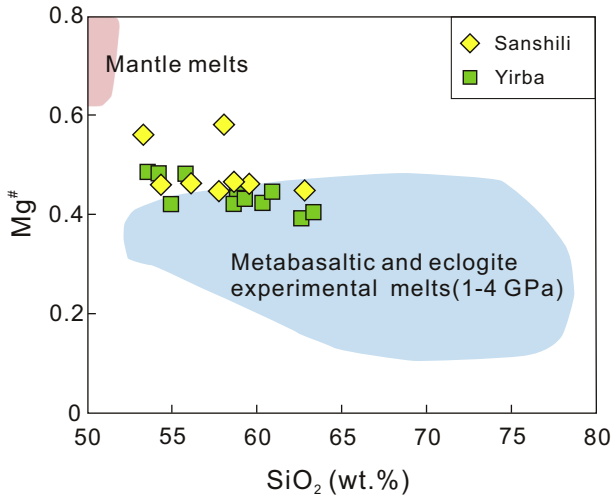

Fig. 11. Mg# versus SiO_2 diagram for samples from the Sanshili and Yirba plutons. The base map is from Wu et al. (2018).

MMEs, some of which have a light-colored transitional zone at the contacting boundary with the host rock (Cui et al., 2006). Cui et al. (2006) also observed higher modal percentages of biotite at the contacting boundary and in enclaves, which was formed during interactions between the enclaves and hydrous K-rich melts that transform amphibole to biotite (Wu et al., 2018). Moreover, there are also some ca.440 Ma mafic dykes with $\varepsilon_{Nd}(t)$ of −2 to −3 in the SKT (Zhang et al., 2019a). These features suggest the hybridization between the host felsic and mafic magmas rather than only fluid additions (Cui et al., 2006).

The Sanshili pluton intruded into the Saitula Group, which was deposited during 600–480 Ma (Zhang et al., 2018b). The volcanic-sedimentary sequence and voluminous 530–400 Ma intrusions in the Saitula Group represent a typical magmatic arc system in the early Paleozoic (Zhang et al., 2018b). Combined with the high oxygen fugacity of the ca.446 Ma zircons and similar Hf isotopic compositions between the inherited zircons and the ca. 446 Ma zircons, we suggest that the Sanshili pluton formed in a subduction-related environment. Specifically, melts derived from the metasomatized mantle wedge underplated into the bottom of the lower crust of the magmatic arc system (as represented by the Saitula Group), triggering partial melting of the heterogeneously lower arc crust, and then mixing between these two kinds of magmas resulting in the formation of the Sanshili pluton. It seems that the lower arc crust is heterogeneously mixed with earlier intrusive rocks. The zircon cores with low Ce^{4+}/Ce^{3+} may represent

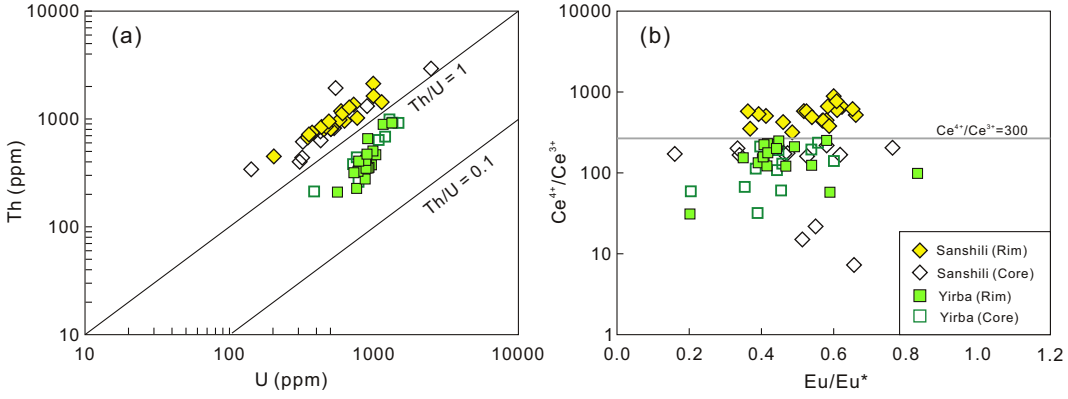

Fig. 10. Trace element compositions for zircon grains in samples from the Sanshili and the Yirba plutons.

crustal components from the crustal magma source, and its ages (546–472 Ma) are consistent with ages of intrusive rocks in the Saitula Group. Furthermore, the metasomatized mantle wedge-derived mafic magmas can act as the oxidized components involved in producing the Sanshili pluton. There is a contemporary calc-alkaline granitic intrusion in the SKT, the Alamas pluton, which is mainly associated with the reworking of an ancient deep crustal source (Zhang et al., 2016a, 2016b). If we take the Sr–Nd isotopic compositions of the metasomatized mantle-derived gabbros (Liu et al., 2019) and the ca. 446 Ma Alamas granitoid to make an estimation, 30–40% contributions from the subduction-modified mantle source are involved in the generation of the Sanshili pluton.

5.2. Petrogenesis of the Yirba pluton

The Yirba pluton has an intermediate to felsic composition with SiO_2 of 53.5–63.3 wt%, and mainly comprises quartz diorite and granodiorite. Samples from the Yirba pluton are also characterized by enriched large ion lithophile elements (LILE) and light rare earth elements (LREE), depleted high field strength elements (HFSE), and high K_2O contents with K_2O/Na_2O. Although the K-enrichment of granitoid can be explained by partial melting of a K_2O-enriched mafic lower crustal source, the possibility of pure crustal melts can be excluded based on their high Mg# (Fig. 11), and the enriched to slightly depleted Hf (Fig. 6) and Nd isotopes (Fig. 9). Specifically, experimental work has shown that partial melting of basaltic rocks can only produce magmas with $Mg^{\#} < 40$ (Rapp and Watson, 1995). However, it is noted that samples from the Yirba pluton have relatively high $Mg^{\#}$ (39–49), and some data are plotted outside of the field defined by experimental melts derived from partial melting of metabasalts and eclogite (Fig. 11). Their high Cr (up to 73.8 ppm) and Ni (up to 27.2 ppm) concentrations and Cr/Ni ratios (2.70–5.43) are also against pure crustal melts derived from partial melting of metabasaltic rocks. Therefore, there are non-negligible mantle contributions in the formation of the Yirba pluton.

Inherited zircon cores can provide important petrogenetic clues that are not identifiable from the whole-rock chemistry. The only slightly higher ε_{Hf} value of the ca. 474 Ma zircons in the host rock than that of the 502–531 Ma zircon cores (projected to the evolution curve at 474 Ma with $^{176}Lu/^{177}Hf = 0.015$: average continental crust) provides compelling evidence of reworking of early igneous rocks (Fig. 6). On the other hand, the Yirba pluton intrudes into the volcanic sequence of the Kudi ophiolite suite (Yixieke Group), which was formed in a supra-subduction zone setting during ca.525–490 Ma, and represents an intra-oceanic island arc (Xiao et al., 2003; Yuan et al., 2003). The ages of those inherited zircon cores (505–532 Ma) are indistinguishable from the formation age of the Kudi ophiolite suite. The ε_{Hf} values of these 505–532 Ma zircon cores are also within the range of zircons from the host granitoids (Fig. 6a). Therefore, the lower crust of the juvenile intra-oceanic arc (formed at ca.525–490 Ma) must have been involved in the generation of the Yirba pluton.

The nature of the magma source is also of great importance in understanding the origin of granitoids. The ca. 474 Ma zircon crystals from the Yirba pluton display lower Ce^{4+}/Ce^{3+} than ca. 446 Ma zircons from the Sanshili pluton. As discussed above, the Sanshili tonalitic and granodioritic rocks are formed by interactions between metasomatized mantle wedge-derived oxidized magma with crust-derived melts. Thus, the low Ce^{4+}/Ce^{3+} ratios of these ca. 474 Ma zircons precludes the possibility that these mantle melts are derived from the metasomatized mantle wedge. Instead, we argue that the mantle-derived components in the Yirba pluton may associate with partial melting of the metasomatized lithospheric mantle beneath the intra-oceanic arc. The Yirba pluton intruded into the intra-oceanic arc, as represented by the Yishake Group (Xiao et al., 2005; Yuan et al., 2002), and samples from the Yirba pluton are characterized by high Th/Nb (Fig. 12b). Previous studies showed that partial melting of subducting sediments is responsible for fractionating Th from Nb, when Th is more incompatible than Nb (Johnson and Plank, 2000). Therefore, the lithospheric mantle might be previously metasomatized by sediment-derived melts during subduction of the Proto-Tethys. Partial melting of the lithospheric mantle metasomatized by sediment-derived melts/fluids can not only explain the high $(^{87}Sr/^{86}Sr)_i$ (0.7052–0.7091) but also account for the high K_2O contents and K_2O/Na_2O ratios of the Yirba pluton (Fu et al., 2018). When we take the Sr–Nd isotopic compositions of the most primitive gabbros (Zhang et al., 2018a) and the ca. 513 Taer granite (with the most enriched Sr–Nd isotopic compositions among the 490–530 Ma granites) (Yin et al., 2020) to make a simple mixing calculation, about 30–55% mantle contributions are required to produce the Yirba pluton.

In summary, the Yirba pluton was generated through differentiation of the metasomatized lithospheric mantle-derived magmas beneath a juvenile intra-oceanic arc together with crustal reworking. As shown in Fig. 12, samples from the Yirba pluton contain higher Y + Nb concentrations than the typical volcanic arc granites, some of which are plotted into the field of within plate granites. Meanwhile, there is increasing Nb/La and Nb/Y in igneous rocks from 490 Ma to 470 Ma (Fig. 13). The Nb/La ratios of average ocean island basalts (1.3) are higher than island arc basalts (0.34 on average) (Sun and Mcdonough, 1989). Since the Nb/La ratio is insensitive to the degree of fractionation, a high Nb/La ratio (>0.71) indicates more contributions from intraplate-like source melts during lithospheric extension (Kemp et al., 2009; Tang et al., 2017). It has also been shown that high Nb/La ratio and depleted Nd–Hf isotopes of granitoids also indicate contributions from intraplate-like sources in the mantle-derived components in granitic rocks (Kemp et al., 2009). Therefore, the Yirba pluton might be formed during regional extension, which is consistent with the occurrence of the

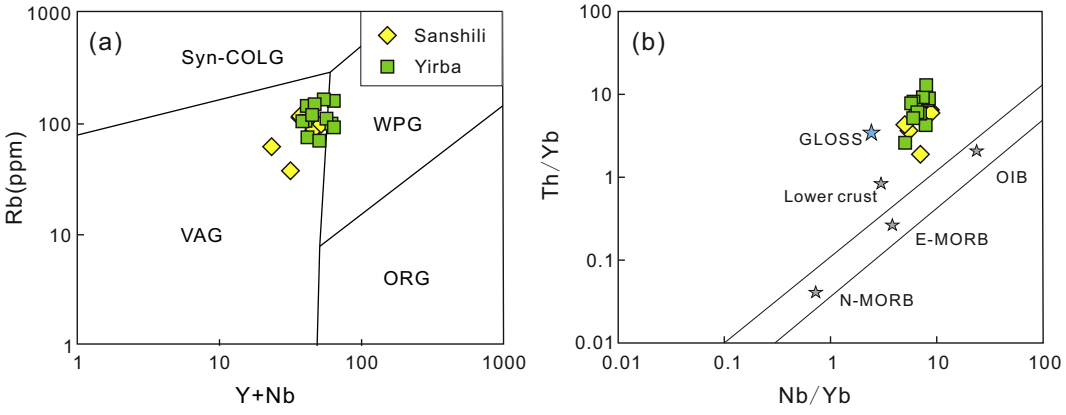

Fig. 12. (a) Rb-Y+Nb and (b) Th/Yb-Nb/Yb diagrams for samples from the Sanshili and Yirba plutons, after Pearce and Peate (1995).

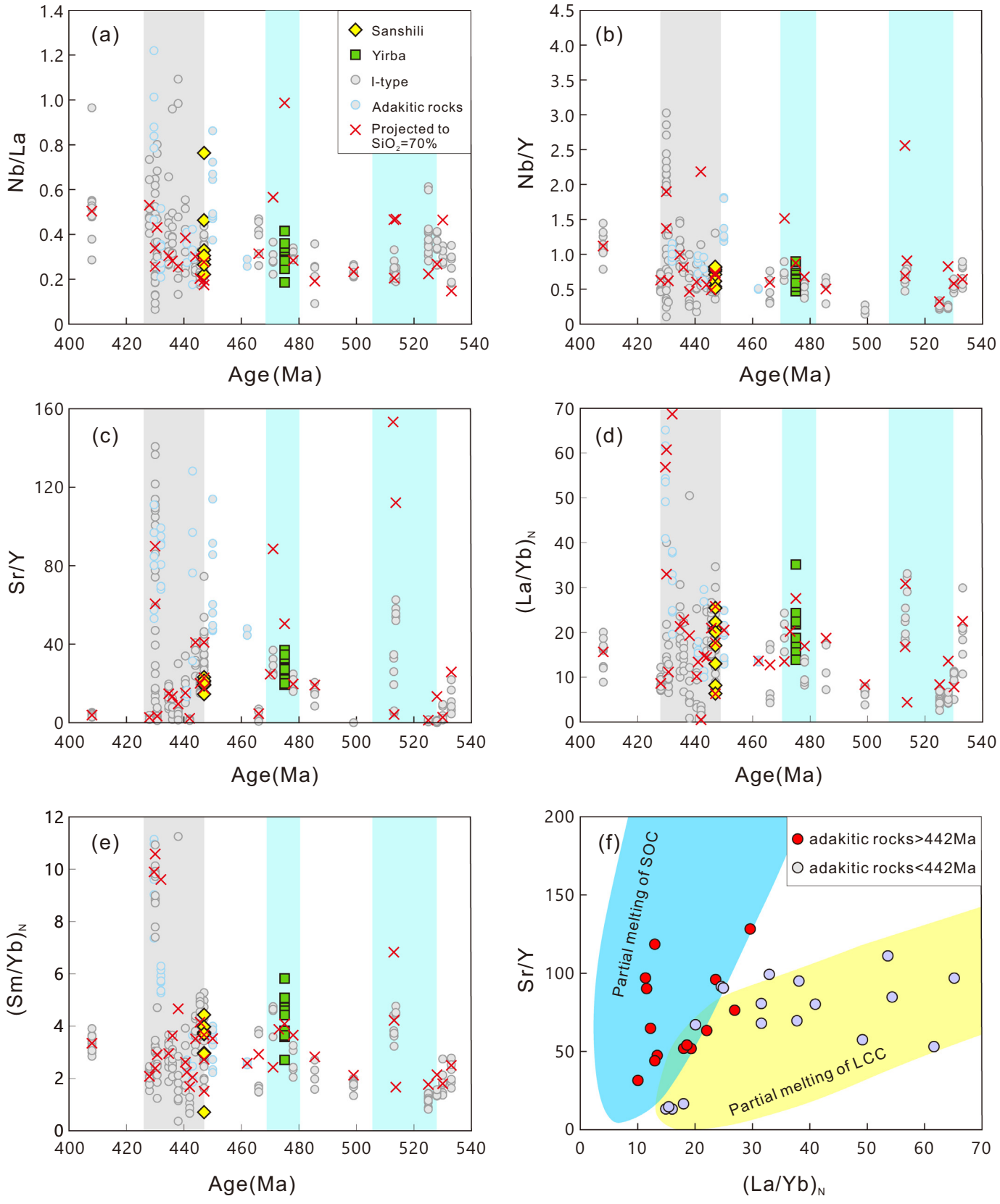

Fig. 13. The Nb/La (a), Nb/Y (b), Sr/Y (c), $(La/Yb)_N$ (d), $(Sm/Yb)_N$ (e) variations through time for the early Paleozoic granitoids from the Western Kunlun orogen, and the Sr/Y versus $(La/Yb)_N$ (f) diagram for the early Paleozoic adakites and adakitic rocks in the Western Kunlun orogen.

ca.471 Ma Kasilafu A_1-type granite in the Datongxi region (Li et al., 2018). The trigger for partial melting of the lithospheric mantle can be ascribed to heat supplied from the upwelling asthenosphere during regional extension. In other words, there should be an extensional event at around 480–470 Ma in the Western Kunlun orogen.

5.3. Linking isotopic changes to geodynamic processes

It is generally accepted that the Western Kunlun orogen is an accretionary orogen during the consumption of the Proto-Tethys (Xiao et al., 2005; Zhang et al., 2018b). However, unlike other accretionary orogens which might be subjected to multiple episodes of extension punctuated by contractional events, there is lacking emphasis on extensional events in the Western Kunlun orogen. This may be partly due to subsequent repeated contractional events that may obliterate those extensional structures. Interestingly, some recent studies recognized an extensional event at 533–514 Ma based on the 521 Ma bimodal volcanic rocks and northward migrations of magmatism during the Cambrian (Yin et al., 2020). This implies that the Western Kunlun orogen should at least be characterized by continuing contractions that were interrupted by extensions. In the following parts, we try to link the changes in Nd–Hf isotopic compositions of the early Paleozoic granitoids to the geodynamic transitions during the evolution of the Western Kunlun Orogen. The data source of the granitoids is available in Table S1.

The tectonic transition between extension and contraction in accretionary orogens is generally ascribed to a change from slab rollback, upper plate extension, and the formation of rift basin and back-arc systems to back-arc closure and flat subduction of buoyant oceanic plateaus (Kemp et al., 2009). An accompanied change in magma sources is also predicted: there should be increasing crustal contributions in arc magmas during advancing subduction, whereas the renewed subduction zone retreat permits asthenosphere upwelling and inputs of juvenile materials. This change is also witnessed by the early Paleozoic granitoids from the Western Kunlun orogen. As shown in Fig. 9, the Sr–Nd isotopes of the early Paleozoic granitic rocks from the Western Kunlun orogen define a hyperbolic curve, which is broadly overprinted by the modeled mixing curve between the gabbros in the SKT and the Precambrian metasedimentary rocks. When plotted against crystallization age, the whole-rock Nd isotopic compositions define a similar trend that was constrained by zircon Hf isotope data (Fig. 6). The $\varepsilon_{Nd}(t)$ and $\varepsilon_{Hf}(t)$ values gradually change from positive to negative after subduction initiation of the Proto-Tethys, and rapidly resume to positive at ca.475 Ma. Then after a quick decrease to strong negative, the $\varepsilon_{Nd}(t)$ and $\varepsilon_{Hf}(t)$ values eventually return to positive values for granitoids formed during the slab-break off after the final closure of the Proto-Tethys (Figs. 6 and 9) (Zhang et al., 2019a).

Changes in $\varepsilon_{Nd}(t)$ and $\varepsilon_{Hf}(t)$ values essentially reflect variations in the magma source, which can be perfectly linked to geodynamic processes during the evolution of the Western Kunlun orogen. After subduction initiation and the first extensional events at 533–514 Ma, the gradually decreasing $\varepsilon_{Nd}(t)$ and $\varepsilon_{Hf}(t)$ values reflect enhanced crustal contributions in the genesis of the early Paleozoic granitic rocks, which may associate with enhanced crust recycling in subduction zones through either increased crustal input or subduction erosion, and/or prolonged assimilation processes when traversing the thickened continental crust during advancing subduction. The decreasing trend ceased at ca.480 Ma, when the Nd and Hf isotopes become radiogenic. As discussed above, contemporaneous granitic rocks contain more intraplate signatures (increased Nb + Y concentrations, and the Nb/La and Nb/Y ratios), which is ascribed to slab rollback and asthenospheric upwelling. Besides, such an extensional event is also in accordance with the occurrence of the 471 Ma A-type granite (Li et al., 2018). Then subduction recommenced after such an extensional event, and heat and fluids derived from arc magmas induced partial melting of thickened metasediments that were deposited during the extensional processes (Wang et al., 2013). In such a scenario, the ca. 455 Ma Kayedi S-type granite was formed shortly after subduction re-initiation (Zhang et al., 2019b). Similar processes also occurred in other accretionary orogens like the Tasmaides orogen and the Lachlan orogen (Kemp et al., 2009). Finally, the Proto-Tethys closed at ca.442 Ma, when slab-derived adakites were replaced by thickened lower crust-derived adakitic rocks (Fig. 13f). The final closure of the Proto-Tethys was followed by slab break-off (Yang et al., 2016), and subsequent asthenosphere upwelling and crust-mantle interactions produced a linear distributed high Sr/Y and high-K granitoid belt within a short time interval (450–430 Ma) (Ye et al., 2008; Zhang et al., 2019a).

5.4. Implications for continental growth in accretionary orogens

Accretionary orogens are traditionally envisaged as the primary site for continental growth, while collisional orogen is invoked as the sites for crustal reworking (Cawood et al., 2009). The additions of mantle-derived juvenile materials into the continental crust can be realized through vertical arc magmatism and lateral accretion of oceanic arcs and plateaus (Taylor and McLennan, 1985). However, the volume of the added continental crust is shown to be effectively compensated by continental crust recycling at plate margins through sediment subduction, subduction erosion, and density foundering of the arc root (Zandt et al., 2004). In contrast, recent studies proposed that juvenile materials are significantly added to the crust during back-arc extension in accretionary orogens, and repeated subduction retreat and advancing events are crucial for rapid continental growth at convergent margins (Collins et al., 2011; Kemp et al., 2009). Meanwhile, it has also been proposed that continental collision zones are the primary sites for net crustal growth (Niu et al., 2013). Although all accretionary orogens contain a collisional phase after the final closure of ocean basins, little effort has been made to evaluate the amount of juvenile crust generation throughout the evolution of an accretionary orogen. Here, we combined our new results on the Sanshili and the Yirba plutons with the available literature geochemical data of the early Paleozoic granitoids to evaluate the rate and amount of crustal growth in the Western Kunlun Orogen.

We apply two groups of trace element ratios to monitor juvenile additions and crustal thickness. The first group comprises the Nb/La and Nb/Y ratios, which are sensitive to changes in intraplate-plate components. High ratios of Nb/La and Nb/Y are typical features of ocean island basalts (OIB), which are associated with plume activities or lithospheric extensions (Sun and Mcdonough, 1989; Tang et al., 2017). The second group refers to $(La/Yb)_N$, $(Sm/Yb)_N$, and Sr/Y, which are generally translated into crustal thickness (Profeta et al., 2015; Tang et al., 2020). During partial melting and fractionation process, Sr is preferentially partitioned into plagioclase at low pressures and into melts at high pressures when plagioclase becomes unstable (Profeta et al., 2015). The rare earth element composition of granitoids is mainly controlled by amphibole and garnet during magmatic differentiation, because these two minerals dominate the budgets of middle and heavy REEs, respectively. It is suggested that high $(Sm/Yb)_N$ (>5) marks garnet-dominated fractionation of granitoids (Balica et al., 2020). Therefore, high $(La/Yb)_N$, $(Sm/Yb)_N$, and Sr/Y ratios reflect enhanced garnet and amphibolite fractionations relative to plagioclase at high pressures, which implies a thick continental crust (Profeta et al., 2015; Tang et al., 2020). Since some trace element ratios (e.g., Sr/Y) might be affected by shallow level fractionation, trace element ratios of each granitic intrusion are plotted with SiO_2, and then projected to $SiO_2 = 70\%$. Differences in differentiation degree in granitoids can be minimized in this way (Tang et al., 2017).

Similar to whole-rock Nd and zircon Hf isotopes, we observed three peaks punctuated by toughs for the selected trace element ratios (Fig. 13), which is coincident with the three magmatic flare-ups in the age frequency distribution diagram of the early Paleozoic granitoids (Fig. 6b). The observed peaks for the Nb/La and Nb/Y ratios imply high proportions of intraplate components and thus enhanced mantle-derived juvenile materials, which are associated with asthenospheric upwelling during subduction retreat. Meanwhile, the crust is also

thickened, as inferred from the high Sr/Y, $(La/Yb)_N$, and $(Sm/Yb)_N$. These phenomena are in accordance with the suggestion that juvenile crust generation in accretionary orogens is intimately bound up with extensional settings.

To evaluate the relative amounts of crust generation, we use the whole-rock Nd isotopic compositions to estimate the factions of juvenile input throughout the evolution of the Western Kunlun orogen, and then estimate the crust generation rates. It is a common approach to choose the isotopic composition of local mafic intrusive rocks as the juvenile endmember, and that of a metasedimentary suit as the crustal ingredient to estimate the relative amounts and rates of continental growth (Kemp et al., 2009; Tang et al., 2017). In this study, we select the most primitive ca.530 Ma gabbros in the SKT (Zhang et al., 2018a) as the juvenile endmember and the Precambrian metasedimentary rocks (Jia et al., 2013) as the crustal endmember to calculate the amount and rate of crustal growth during the evolution of the Western Kunlun orogen. Although such calculation cannot precisely explain the origin of each granitic intrusion, it can give a sense of overall changes in the amount and rate of crustal growth. The mixing model indicates that the proportion of juvenile materials in these early Paleozoic granitoids varies from 20% to 87%, with >50% juvenile inputs during magmatic flare-ups (Fig. 14). For comparisons, we also use zircon Hf isotopes to make the calculation. The crustal endmember and the juvenile endmember are set as points with the oldest ($\varepsilon_{Hf} = -17.5$) and

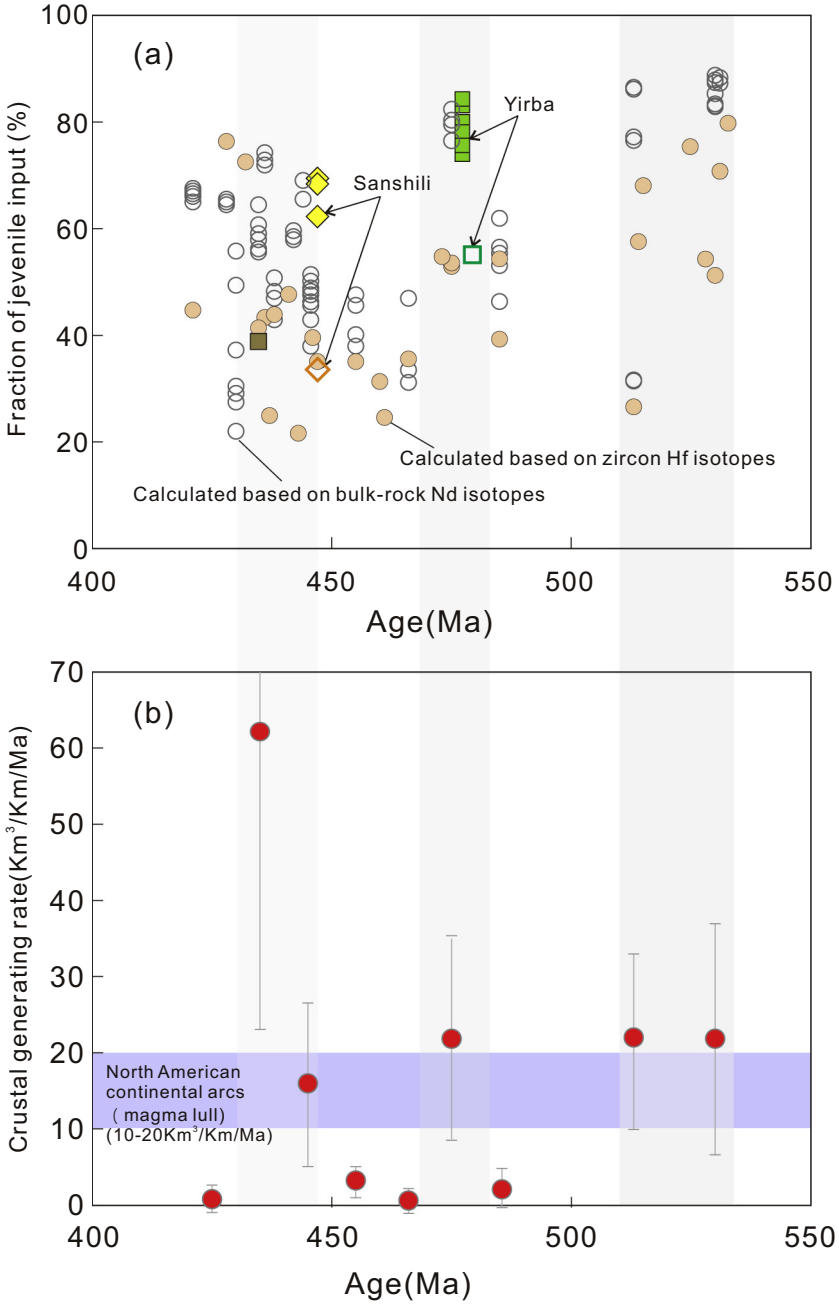

Fig. 14. (a) Changes in the fraction of juvenile input in the early Paleozoic granitoids from the Western Kunlun orogen through time, calculated based on bulk-rock Nd isotopes and zircon Hf isotopes. (b) Estimated crust generation rates (km^3/km/Ma) through time for the Western Kunlun orogen using the Nd isotopic compositions of the early Paleozoic granitoids. The rate for North American continental arc (magmatic lulls) is from Holbrook et al. (1999). The length of the arc segments is estimated to be ca. 500 km based on the distributions of the early Paleozoic granitoids in the Western Kunlun orogen, and the granite crustal thickness is assumed to be 15 ± 10 km, which is considered as the average granite crustal thickness (Tang et al., 2017).

youngest ($\varepsilon_{Hf} = 13$) T_{DM2} in Fig. 6. The calculation suggests that about 22% to 80% juvenile inputs were involved in the generation of the early Paleozoic granitoids in the Western Kunlun orogen, which is broadly consistent with the results on basis of whole-rock Nd isotopes. It is also noted that although the juvenile inputs in granitoids formed during slab rollback are higher than those formed during the final slab break-off event after the closure of the Proto-Tethys, the crustal generating rate during slab rollback is much lower. A plausible explanation for this phenomenon would be extra inputs from partial melting of oceanic slabs and subducting sediments like those in continental collision zones, and/or rapid asthenospheric upwelling and enhanced crust reworking during slab break-off. The crustal generating rates during the three magmatic flare-ups are higher than the current magma generation rates during magma lull in the North American continental margin (Fig. 14b), and the maximum value during the slab break-off is approaching the magma generation rates for an intra-oceanic arc (40–180 km^3/km/Ma) (Tang et al., 2017). This highlights the fact that a significant amount of juvenile crust is generated in extensional accretionary orogens.

6. Conclusions

(1) The ca.446 Ma Sanshili pluton was formed by interactions between the metasomatized mantle wedge-derived mafic magmas and the lower arc crust. The ca.474 Ma Yirba pluton is formed under an extensional setting.
(2) The complied granitoid dataset reveals three episodes of intensive magmatism at 520–500 Ma, 480–470 Ma, and 445–430 Ma in the Western Kunlun orogen, which corresponds to two slab rollback events and the slab break-off after the final closure of the Proto-Tethys.
(3) Crustal growth in accretionary orogens is intimately linked to regional extensions, but the crust generating rate is relatively uniform for different extensional events. The crustal generating rate during the slab break-off event is much higher than that during slab rollback for the Western Kunlun orogen, although the proportions of juvenile inputs in granitoids formed during slab rollback are higher.

Declaration of Competing Interest

We declare that we do not have any commercial or associative interest that represents a conflict of interest in connection with the work submitted.

Acknowledgment

We would like to thank Prof. Greg Shellnutt for his careful editorial handling. We are grateful for the constructive comments from two anonymous reviewers. This study was supported by the National Natural Science Foundation of China (Grants 41903009, 41825007 and 41703027) and China Postdoctoral Science Foundation Grant (2018M643711). We thank Ying Liu, Shenglin Sun, Fang Liu and Le Zhang at Guangzhou Institute of Geochemistry, Chinese Academy of Sciences for their help in the experimental work.

Appendix A. Supplementary data

Supplementary data to this article can be found online at https://doi.org/10.1016/j.lithos.2021.106253.

References

Balica, C., Ducea, M.N., Gehrels, G.E., Kirk, J., Roban, R.D., Luffi, P., Chapman, J.B., Triantafyllou, A., Guo, J., Stoica, A.M., Ruiz, J., Balintoni, I., Profeta, L., Hoffman, D., Petrescu, L., 2020. A zircon petrochronologic view on granitoids and continental evolution. Earth Planet. Sci. Lett. 531, 1–6.
Ballard, J.R., Palin, M.J., Campbell, I.H., 2002. Relative oxidation states of magmas inferred from Ce (IV)/Ce (III) in zircon: application to porphyry copper deposits of northern Chile. Contrib. Mineral. Petrol. 144, 347–364.
Bouvier, A., Vervoort, J.D., Patchett, P.J., 2008. The Lu–Hf and Sm–Nd isotopic composition of CHUR: constraints from unequilibrated chondrites and implications for the bulk composition of terrestrial planets. Earth Planet. Sci. Lett. 273, 48–57.
Cawood, P.A., Kröner, A., Collins, W.J., Kusky, T.M., Mooney, W.D., Windley, B.F., 2009. Accretionary orogens through Earth history. Geol. Soc. Lond., Spec. Publ. 318, 1–36.
Cawood, P.A., Hawkesworth, C.J., Dhuime, B., 2013. The continental record and the generation of continental crust. Bulletin 125, 14–32.
Collins, W.J., 2002. Hot orogens, tectonic switching, and creation of continental crust. Geology 30, 535–538.
Collins, W.J., Belousova, E.A., Kemp, A.I., Murphy, J.B., 2011. Two contrasting Phanerozoic orogenic systems revealed by hafnium isotope data. Nat. Geosci. 4, 333–337.
Collins, W.J., Huang, H.Q., Jiang, X.Y., 2016. Water-fluxed crustal melting produces Cordilleran batholiths. Geology 44, 143–146.
Cui, J.T., Wang, J.C., Bian, X.W., Zhu, H.P., 2006. Geological characteristics of early Paleozoic quartz diorite in the vicinity of Kangxiwar, West Kunlun, China and its zircon SHRIMP U-Pb dating. Geol. Bull. China 25, 1450–1457 (In Chinese with English abstract).
Cui, J.T., Wang, J.C., Bian, X.W., Luo, Q.Z., Zhu, H.P., Wang, M.C., Chen, G.C., 2007a. Zircon SHRIMP U-Pb dating of the Dongbake gneissic tonalite in northern Kangxiwar, West Kunlun. Geol. Bull. China 26, 726–729 (In Chinese with English abstract).
Cui, J.T., Wang, J.C., Bian, X.W., Zhu, H.P., Luo, Q.Z., Yang, K.J., Wang, M.C., 2007b. Zircon SHRIMP U-Pb dating of early Paleozoic granite in the Menggubao-Pushou area on the northern side of Kangxiwar, West Kunlun. Geol. Bull. China 26, 710–719 (In Chinese with English abstract).
Davies, J.H., von Blanckenburg, F., 1995. Slab break-off: a model of lithosphere detachment and its test in the magmatism and deformation of collisional orogens. Earth Planet. Sci. Lett. 129, 85–102.
Dhuime, B., Hawkesworth, C.J., Delavault, H., Cawood, P.A., 2018. Rates of generation and destruction of the continental crust: implications for continental growth. Philos. Trans. R. Soc. A Math. Phys. Eng. Sci. 376, 1–11.
Fu, D., Kusky, T., Wilde, S.A., Polat, A., Huang, B., Zhou, Z., 2018. Early Paleozoic collision-related magmatism in the eastern North Qilian orogen, northern Tibet: a linkage between accretionary and collisional orogenesis. GSA Bull. 131, 1031–1056.
Han, F.L., Cui, J.T., Ji, W.H., Li, H.P., Hao, J.W., 2002. Discovery of the Qimanyute ophiolite in the West Kunlun and its geological significance. Geol. Bull. China 21, 573–578.
Hawkesworth, C., Cawood, P.A., Dhuime, B., 2019. Rates of generation and growth of the continental crust. Geosci. Front. 10, 165–173.
Holbrook, W.S., Lizarralde, D., Mcgeary, S., Bangs, N.L., Diebold, J.B., 1999. Structure and composition of the Aleutian island arc and implications for continental crustal growth. Geology 27, 31–34.
Hoskin, P.W.O., Schaltegger, U., 2003. The composition of zircon and igneous and metamorphic petrogenesis. In: Hanchar, J.M., Hoskin, P.W.O. (Eds.), Zircon. Mineralogical Soc America, Washington, pp. 27–62.
Hu, J., Wang, H., Huang, C.Y., Tong, L.X., Mu, S.L., Qiu, Z.W., 2016. Geological characteristics and age of the Dahongliutan Fe-ore deposit in the Western Kunlun orogenic belt, Xinjiang, northwestern China. J. Asian Earth Sci. 116, 1–25.
Hu, J., Wang, H., Mu, S.L., Wang, M., Hou, X.W., 2017. Geochemistry and Hf isotopic compositions of early Paleozoic granites in Nanpingxueshan from the Tianshuihai Terrane, West Kunlun: Crust-Mantle magmatism. Acta Geol. Sin. 91, 1192–1207 (In Chinese with English abstract).
Jia, R.Y., Jiang, Y.H., Liu, Z., Zhao, P., Zhou, Q., 2013. Petrogenesis and tectonic implications of early Silurian high-K calc-alkaline granites and their potassic microgranular enclaves, western Kunlun orogen, NW Tibetan Plateau. Int. Geol. Rev. 55, 958–975.
Jiang, Y.H., Rui, X.J., He, J.R., Guo, D.Y., Yang, W.Z., 1999. Tectonic type of Caledonian granitoids and tectonic significance in the West Kunlun Mts. Acta Petrol. Sin. 15, 105–115 (In Chinese with English abstract).
Johnson, M.C., Plank, T., 2000. Dehydration and melting experiments constrain the fate of subducted sediments. Geochem. Geophys. Geosyst. 1.
Kelemen, P.B., Behn, M.D., 2016. Formation of lower continental crust by relamination of buoyant arc lavas and plutons. Nat. Geosci. 9, 197–205.
Kemp, A.I.S., Hawkesworth, C.J., Collins, W.J., Gray, C.M., Blevin, P.L., 2009. Isotopic evidence for rapid continental growth in an extensional accretionary orogen: the Tasmanides, eastern Australia. Earth Planet. Sci. Lett. 284, 455–466.
Li, T.F., Zhang, J.X., 2014. Zircon LA-ICP-MS U-Pb ages of websterite and basalt in Kudi ophiolite and the implication, West Kunlun. Acta Petrol. Sin. 30, 2393–2401 (In Chinese with English abstract).
Li, B.Q., Ji, W.H., Bian, X.W., Wang, F., Li, W., 2007. The composition and geological significance of the Mazha Tectonic Melange in West Kunlun Mountains. Geoscience 21, 78–86 (In Chinese with English abstract).
Li, H., Ling, M.X., Li, C.Y., Zhang, H., Ding, X., Yang, X.Y., Fan, W.M., Li, Y.L., Sun, W.D., 2012. A-type granite belts of two chemical subgroups in central eastern China: Indication of ridge subduction. Lithos 150, 26–36.
Li, X.H., Tang, G.Q., Gong, B., Yang, Y.H., Hou, K.J., Hu, Z.C., Li, Q.L., Liu, Y., Li, W.X., 2013. Qinghu zircon: a working reference for microbeam analysis of U-Pb age and Hf and O isotopes. Chin. Sci. Bull. 58, 4647–4654.
Li, Y.C., Xiao, W.J., Tian, Z.H., 2018. Early Palaeozoic accretionary tectonics of West Kunlun Orogen: Insights from Datong granitoids, mafic–ultramafic complexes, and Silurian–Devonian sandstones, Xinjiang, NW China. Geol. J. 54, 1505–1517.
Liang, X.R., Wei, G.J., Li, X.H., Liu, Y., 2003. Precise measurement of 143Nd/144Nd and Sm/Nd ratios using multiple-collectors inductively coupled plasma-mass spectrometer (MC-ICPMS). Geochimica 32, 91–96.

Liao, S.Y., Jiang, Y.H., Jiang, S.Y., Yang, W.Z., Zhou, Q., Jin, G.D., Zhao, P., 2010. Subducting sediment-derived arc granitoids: evidence from the Datong pluton and its quenched enclaves in the western Kunlun orogen, Northwest China. Mineral. Petrol. 100, 55–74.
Liu, Y.S., Hu, Z.C., Gao, S., Günther, D., Xu, J., Gao, C.G., Chen, H.H., 2008. In situ analysis of major and trace elements of anhydrous minerals by LA-ICP-MS without applying an internal standard. Chem. Geol. 257, 34–43.
Liu, Z., Jiang, Y.H., Jia, R.Y., Zhao, P., Zhou, Q., Wang, G.C., Ni, C.Y., 2014. Origin of Middle Cambrian and late Silurian potassic granitoids from the western Kunlun orogen, Northwest China: a magmatic response to the Proto-Tethys evolution. Mineral. Petrol. 108, 91–110.
Liu, X.Q., Zhang, C.L., Ye, X.T., Zou, H.b., Hao, X.S., 2019. Cambrian mafic and granitic intrusions in the Mazar-Tianshuihai terrane, West Kunlun Orogenic Belt: Constraints on the subduction orientation of the Proto-Tethys Ocean. Lithos 350–351.
Moyen, J.F., Laurent, O., Chelle-Michou, C., Couzinié, S., Vanderhaeghe, O., Zeh, A., Villaros, A., Gardien, V., 2017. Collision vs. subduction-related magmatism: two contrasting ways of granite formation and implications for crustal growth. Lithos 277, 154–177.
Niu, Y.L., Zhao, Z.D., Zhu, D.C., Mo, X.X., 2013. Continental collision zones are primary sites for net continental crust growth—a testable hypothesis. Earth Sci. Rev. 127, 96–110.
Pearce, J.A., Peate, D.W., 1995. Tectonic implications of the composition of volcanic arc magmas. Annu. Rev. Earth Planet. Sci. 23, 251–286.
Profeta, L., Ducea, M.N., Chapman, J.B., Paterson, S.R., Gonzales, S.M.H., Kirsch, M., Petrescu, L., Decelles, P.G., 2015. Quantifying crustal thickness over time in magmatic arcs. Sci. Rep. 5 (serp 17786), 1–7.
Rapp, R.P., Watson, E.B., 1995. Dehydration melting of metabasalt at 8–32 kbar: implications for continental growth and crust-mantle recycling. J. Petrol. 36, 891–931.
Rudnick, R.L., Gao, S., 2003. Composition of the continental crust. The Crust 3, 1–64.
Sláma, J., Košler, J., Condon, D.J., Crowley, J.L., Gerdes, A., Hanchar, J.M., Horstwood, M.S., Morris, G.A., Nasdala, L., Norberg, N., 2008. Plešovice zircon—a new natural reference material for U–Pb and Hf isotopic microanalysis. Chem. Geol. 249, 1–35.
Sun, S.S., Mcdonough, W.F., 1989. Chemical and isotopic systematics of oceanic basalts: implications for mantle composition and processes. Geol. Soc. Lond., Spec. Publ. 42, 313–345.
Tang, G.J., Chung, S.L., Hawkesworth, C.J., Cawood, P.A., Wang, Q., Wyman, D.A., Xu, Y.G., Zhao, Z.H., 2017. Short episodes of crust generation during protracted accretionary processes: evidence from Central Asian Orogenic Belt, NW China. Earth Planet. Sci. Lett. 464, 142–154.
Tang, M., Ji, W.Q., Chu, X., Wu, A.B., Chen, C., 2020. Reconstructing crustal thickness evolution from europium anomalies in detrital zircons. Geology 49, 76–80.
Taylor, S.R., McLennan, S.M., 1985. The Continental Crust: Its Composition and Evolution. p. 312.
Trail, D., Watson, E.B., Tailby, N.D., 2012. Ce and Eu anomalies in zircon as proxies for the oxidation state of magmas. Geochim. Cosmochim. Acta 97, 70–87.
Wang, C., Liu, L., He, S.P., Yang, W.Q., Cao, Y.T., Zhu, X.H., Li, R.S., 2013. Early Paleozoic magmatism in west Kunlun: Constraints from geochemical and zircon U-Pb-Hf isotopic studies of the Bulong granite. Chinese J. Geol. 48, 997–1014 (In Chinese with English abstract).
Wang, J., Hattori, K., Liu, J.G., Song, Y., Gao, Y.B., Zhang, H., 2017. Shoshonitic- and adakitic magmatism of the early Paleozoic age in the Western Kunlun orogenic belt, NW China: Implications for the early evolution of the northwestern Tibetan plateau. Lithos 286-287, 345–362.
Wang, P., Zhao, G.C., Han, Y.G., Liu, Q., Zhou, N.C., Yao, J.L., Li, J.H., Li, Y., 2020. Post-collisional potassic rocks in Western Kunlun, NW Tibet Plateau: Insights into lateral variations in the crust-mantle structure beneath the India-Asia collision zone. Lithos 370–371.
Wei, G.J., Liang, X.R., Li, X.H., Liu, Y., 2002. Precise measurement of Sr isotopic composition of liquid and solid base using (LP) MC-ICPMS. Geochimica 31, 295–299.
Wu, K., Ling, M.X., Hu, Y.B., Guo, J., Jiang, X.Y., Sun, S.J., Liang, H.Y., Liu, X., Sun, W., 2018. Melt-Fluxed Melting of the Heterogeneously mixed lower Arc Crust: a Case Study from the Qinling Orogenic Belt, Central China. Geochem. Geophys. Geosyst. 19, 1767–1788.
Xiao, W.J., Han, F.L., Windley, B.F., Yuan, C., Zhou, H., Li, J.L., 2003. Multiple accretionary orogenesis and episodic growth of continents: Insights from the Western Kunlun Range, Central Asia. Int. Geol. Rev. 45, 303–328.
Xiao, W.J., Windley, B.F., Liu, D.Y., Jian, P., Liu, C.Z., Yuan, C., Sun, M., 2005. Accretionary tectonics of the Western Kunlun Orogen, China: a Paleozoic–early Mesozoic, long-lived active continental margin with implications for the growth of Southern Eurasia. J. Geol. 113, 687–705.
Yang, W.Q., Liu, L., Cao, Y.T., Wang, C., He, S.P., Li, R.S., Zhu, X.H., 2010. Geochronological evidence of Indosinian (high-pressure) metamorphic event and its tectonic significance in Taxkorgan area of the Western Kunlun Mountains, NW China. Sci. China Earth Sci. 53, 1445–1459.
Yang, S., Lyn, H.W., Qu, X.X., Lin, Y., Zeng, Z.C., Gao, C., 2016. The discovery of Early-Middle Silurian adakite in West Kunlun Mountains and its geological implications. Acta Petrol. Mineral. 35, 563–578 (In Chinese with English abstract).
Ye, H.M., Li, X.H., Li, Z.X., Zhang, C.L., 2008. Age and origin of high Ba–Sr appinite–granites at the northwestern margin of the Tibet Plateau: implications for early Paleozoic tectonic evolution of the Western Kunlun orogenic belt. Gondwana Res. 13, 126–138.
Yin, J.Y., Xiao, W.J., Sun, M., Chen, W., Yuan, C., Zhang, Y.Y., Wang, T., Du, Q.Y., Wang, X.S., Xia, X.P., 2020. Petrogenesis of early Cambrian granitoids in the western Kunlun orogenic belt, Northwest Tibet: Insight into early stage subduction of the Proto-Tethys Ocean. Geol. Soc. Am. Bull. 132, 2221–2240.
Yu, X.F., Sun, F.Y., Li, B.L., Ding, Q.F., Chen, G.J., Ding, Z.J., Chen, J., Huo, L., 2011. Caledonian diagenetic and metallogenic events in Datong district in the western Kunlun: Evidences from LA-ICP-MS zircon U-Pb dating and molybdenite Re-Os dating. Acta Petrol. Sin. 27, 1770–1778 (In Chinese with English abstract).
Yuan, C., Sun, M., Zhou, M.F., Zhou, H., Xiao, W.J., Li, J.L., 2002. Tectonic evolution of the West Kunlun: geochronologic and geochemical constraints from Kudi Granitoids. Int. Geol. Rev. 44, 653–669.
Yuan, C., Sun, M., Xiao, W.J., Zhou, H., Hou, Q.L., Li, J.L., 2003. Subduction polarity of the prototethys: insights from the Yirba pluton of the western Kunlun range, NW China. Acta Petrol. Sin. 19, 399–408 (In Chinese with English abstract).
Yuan, C., Sun, M., Zhou, M.F., Xiao, W.J., Zhou, H., 2005. Geochemistry and petrogenesis of the Yishak Volcanic Sequence, Kudi ophiolite, West Kunlun (NW China): implications for the magmatic evolution in a subduction zone environment. Contrib. Mineral. Petrol. 150, 195–211.
Zandt, G., Gilbert, H., Owens, T.J., Ducea, M., Saleeby, J., Jones, C.H., 2004. Active foundering of a continental arc root beneath the southern Sierra Nevada in California. Nature 431, 41–46.
Zhang, C.L., Lu, S.N., Yu, H.F., Ye, H.M., 2007. Tectonic evolution of the Western Kunlun orogenic belt in northern Qinghai-Tibet Plateau: evidence from zircon SHRIMP and LA-ICP-MS U-Pb geochronology. Sci. China Ser. D Earth Sci. 50, 825–835.
Zhang, L., Ren, Z.Y., Xia, X.P., Li, J., Zhang, Z.H., 2015. IsotopeMaker: a Matlab program for isotopic data reduction. Int. J. Mass Spectrom. 392, 118–124.
Zhang, H.S., He, S.P., Ji, W.H., Wang, C., Shi, J.B., Kang, K.Y., Zhang, J., Zhu, D.W., Tang, H.W., Li, C.D., Xi, D.H., 2016a. Implications of late Cambrian granite in Tishanshuihai Massif for the evolution of Proto-Tethys Ocean: evidences from zircon geochronology and geochemistry. Acta Geol. Sin. 90, 2582–2602 (In Chinese with English abstract).
Zhang, Q.C., Liu, Y., Huang, H., Wu, Z.H., Zhou, Q., 2016b. Petrogenesis and tectonic implications of the high-K Alamas calc-alkaline granitoids at the northwestern margin of the Tibetan Plateau: Geochemical and Sr–Nd–Hf–O isotope constraints. J. Asian Earth Sci. 127, 137–151.
Zhang, L., Long, X.P., Zhang, R., Dong, Y.P., Yuan, C., Xiao, W.J., Wang, Y.J., 2017. Source characteristics and provenance of metasedimentary rocks from the Kangxiwa Group in the Western Kunlun Orogenic Belt, NW China: Implications for tectonic setting and crustal growth. Gondwana Res. 46, 43–56.
Zhang, C., Zou, H.B., Ye, X.T., Chen, X.Y., 2018a. Timing of subduction initiation in the Proto-Tethys Ocean: evidence from the Cambrian gabbros from the NE Pamir Plateau. Lithos 314, 40–51.
Zhang, C.L., Zou, H.B., Ye, X.T., Chen, X.Y., 2018b. Tectonic evolution of the West Kunlun Orogenic Belt along the northern margin of the Tibetan Plateau: implications for the assembly of the Tarim terrane to Gondwana. Geosci. Front. 10, 973–988.
Zhang, Q.C., Wu, Z.H., Chen, X.H., Zhou, Q., Shen, N.P., 2019a. Proto-Tethys oceanic slab break-off: Insights from early Paleozoic magmatic diversity in the West Kunlun Orogen, NW Tibetan Plateau. Lithos 346, 105–147.
Zhang, Q.C., Wu, Z.N., Li, S., Li, K., Liu, Z.W., 2019b. Ordovician Granitoids and Silurian Mafic Dikes in the Western Kunlun Orogen, Northwest China: Implications for Evolution of the Proto-Tethys. Acta Geol. Sinica-English Ed. 93, 30–49.
Zhu, J., Liu, Q.G., Wang, Z.Q., Tang, H.S., Chen, X., Xiao, B., 2016. Magmatism and Tectonic implications of early Cambrian Granitoid plutons in Tishanshuihai Terrne of the Western Kunlun Orogenic belt, Northwest China. Northwest. Geol. 49, 1–18 (In Chinese with English abstract).
Zhu, J., Li, Q.G., Chen, X., Tang, H.S., Wang, Z.Q., Chen, Y.J., Liu, S.W., Xiao, B., Chen, J.L., 2018. Geochemistry and petrogenesis of the early Palaeozoic appinite-granite complex in the Western Kunlun Orogenic Belt, NW China: implications for Palaeozoic tectonic evolution. Geol. Mag. 155, 1641–1666.